energies

MDPI

Review

Low-Loss Soft Magnetic Materials and Their Application in Power Conversion: Progress and Perspective

Weiwang Wang [1,*], Jiaqi Fan [1], Changshen Li [1], Yue Yu [1], Anding Wang [2], Shengtao Li [1] and Jinjun Liu [1]

[1] State Key Laboratory of Electric Insulation and Power Equipment, Xi'an Jiaotong University, Xi'an 710049, China; fjq15130227544@stu.xjtu.edu.cn (J.F.); Changshen_li@stu.xjtu.edu.cn (C.L.); yuyue2022@stu.xjtu.edu.cn (Y.Y.); sli@xjtu.edu.cn (S.L.); jjliu@xjtu.edu.cn (J.L.)

[2] Research Institute of Interdisciplinary Science, Dongguan University of Technology, Dongguan 523808, China; anding.w@dgut.edu.cn

* Correspondence: weiwwang@xjtu.edu.cn

Abstract: Amorphous and nanocrystalline alloys, as novel soft magnetic materials, can enable high efficiency in a wide range of power conversion techniques. Their wide application requires a thorough understanding of the fundamental material mechanisms, typical characteristics, device design, and applications. The first part of this review briefly overviews the development of amorphous and nanocrystalline alloys, including the structures of soft magnetic composites (SMCs), the key performance, and the underlying property-structure correction mechanisms. The second part discusses three kinds of high-power conversion applications of amorphous and nanocrystalline alloys, such as power electronics transformers (PETs), high-power inductors, and high-power electric motors. Further detailed analysis of these materials and applications are reviewed. Finally, some critical issues and future challenges for material tailoring, device design, and power conversion application are also highlighted.

Keywords: soft magnetic material; amorphous alloy; nanocrystalline alloy; power conversion; transformer; inductor; electric motor; power loss

check for updates

Academic Editor: Yiannis Deligiannakis

Received: 2 December 2024
Revised: 6 January 2025
Accepted: 20 January 2025
Published: 22 January 2025

Citation: Wang, W.; Fan, J.; Li, C.; Yu, Y.; Wang, A.; Li, S.; Liu, J. Low-Loss Soft Magnetic Materials and Their Application in Power Conversion: Progress and Perspective. *Energies* **2025**, *18*, 482. https://doi.org/10.3390/en18030482

Copyright: © 2025 by the authors. Licensee MDPI, Basel, Switzerland. This article is an open access article distributed under the terms and conditions of the Creative Commons Attribution (CC BY) license (https://creativecommons.org/licenses/by/4.0/).

1. Introduction

Energy conversion is witnessing an irreversible trend towards the energy internet for sustainability and efficiency [1]. New power equipment, such as power electronic converters, play a pivotal role in harnessing wind, solar, and hydraulic energies, as well as securing the stable operation of power systems. In recent years, the advance of wide band gap semiconductors has brought in a revolution to higher frequency and higher efficiency [2]. However, existing power devices with bulky sizes and heavy weights fail to meet the development. The magnetic power cores with soft magnetic materials occupy the most space and mass of power components and their auxiliary systems. The selection of soft magnetic materials is of special significance for striking a balance between cost and efficiency [3].

Several types of soft magnetic materials have been developed sequentially for greater compactness and better electrical and magnetic characteristics. Additionally, a number of compound soft magnetic materials with comprehensive striking performance have been produced. Currently, amorphous and nanocrystalline materials exhibit the most attractive application prospects.

High-efficient soft magnetic materials are selected according to the property requirements and servicing environments of the core, which is a complicated procedure for

minimizing size, loss, leakage inductance, local heating, and vibration. Moreover, the production techniques for ribbon materials have evolved many times, playing an essential role in securing their overall performance.

Nowadays, soft magnetic materials have been widely applied to various high-power conversion scenarios and magnetic devices in power electronics, as shown in Figure 1, including high-power transformers, inductors, motors, and common mode chokes for mitigating electromagnetic interference (EMI). Amorphous and nanocrystalline alloys offer low core losses, high saturation flux densities, and excellent permeability, making them ideal for applications where efficiency and size reductions are critical, while other soft magnetic materials, such as silicon steel and ferrite, do not offer both low core loss and high efficiency, especially at high frequency. Magnetic ribbons, especially amorphous and nanocrystalline ribbons, play a crucial role in the development of soft magnetic materials due to their excellent magnetic properties and reduced energy losses. Among the various synthesis methods, melt spinning has emerged as a widely adopted and efficient technique for fabricating magnetic ribbons. This method involves rapidly cooling a molten alloy onto a rotating copper wheel, resulting in a thin ribbon with amorphous or nanocrystalline structures. Melt spinning not only provides high efficiency in ribbon synthesis but also allows precise control over microstructural and magnetic characteristics [4,5]. This technique is particularly suitable for the production of ribbons with high saturation magnetization, low coercivity, and excellent permeability.



Figure 1. Application scenarios of nanocomposite.

This paper aims to discuss the advances in soft magnetic materials, especially for amorphous and nanocrystalline alloys, and the prospects of their significant applications in power conversion. The paper is presented as follows. In Section 2, the classification of soft magnetic materials and a well-rounded comparison of their properties are explored and discussed. Subsequently, the mechanisms underlying the amorphous and nanocrystalline materials are extrapolated. Moreover, the correlation between different engineering techniques (i.e., from the composition optimization to external treatment) and the resulting properties are revealed. Key issues and the development of amorphous and nanocrystalline materials are introduced. Sections 3 and 4 discuss the application of soft magnetic materials in high-power-density transformers and inductors. The following structure contains the specific requirements of electromagnetic properties of magnetic cores, the design optimization, and the comprehensive analysis of the power device. The operation conditions related to soft magnetic ribbon materials include temperature rise, vibration, and insulation issues. In Section 5, an evolution of high-power motors is introduced, followed by the particular request for soft magnetic materials and the analysis and optimization of manufacturing and operation processes. In Section 6, concluding remarks on the research status are summarized, and the perspective for the development of amorphous and nanocrystalline materials

alongside their applications is separated into three parts. It highlights the short-term, intermediate-term, and long-term development of soft magnetic ribbon material.

2. An Overview of Soft Magnetic Materials

2.1. Magnetic Characteristics

Soft magnetic materials can be roughly separated into three kinds: soft ferrites, composed of oxides based on Fe, Ni, Zn, Mn, and their combinations (MnZn and NiZn), are bulk materials with high electric resistance; bulk crystalline alloys with grain sizes of 10 μm to 10 mm, such as FeSi, FeNi, and FeCo alloys; amorphous and nanocrystalline alloy ribbons manufactured effectively by plane flow casting technique. The former two kinds are technologically mature in manufacture and applications. Therefore, this paper focuses on amorphous and nanocrystalline alloys.

Permeability is a critical parameter that affects electromagnetic properties and practical applications. It describes the ability of a material to respond to an applied magnetic field. Experimental measurements of permeability typically involve impedance analysis, the hysteresis loop method, and the resonance method. The impedance analysis method is widely used for high-frequency permeability measurement. By employing an impedance analyzer to test the impedance of core materials at various frequencies, it is possible to extract both the real and imaginary parts of the complex permeability. It is used to analyze hysteresis and eddy current losses. The hysteresis loop method determines the initial permeability and maximum permeability by recording the relationship between the applied magnetic field and magnetization. It is more applicable for the evaluation of magnetic materials under low-frequency or DC conditions. The resonance method is used to measure the resonance frequency and quality factor of the sample, especially for high-frequency applications. The permeability can be precisely extracted, making this method widely used in the study of nanoscale magnetic materials.

Figure 2 shows the dependence of saturation magnetization on the frequency of different materials. Metal amorphous nanocomposite (MANC) alloys represent a new class of metal/oxide nanocomposites, characterized by the incorporation of oxide phases within a metallic matrix. This unique structure enhances mechanical, magnetic, and thermal properties by leveraging the synergistic effects between the metal and oxide components [6]. Recent advancements, as depicted in Figure 2, include the optimization of ribbon thinning and alloy chemistries, which are pivotal for the development of next-generation MANC-based materials [7].

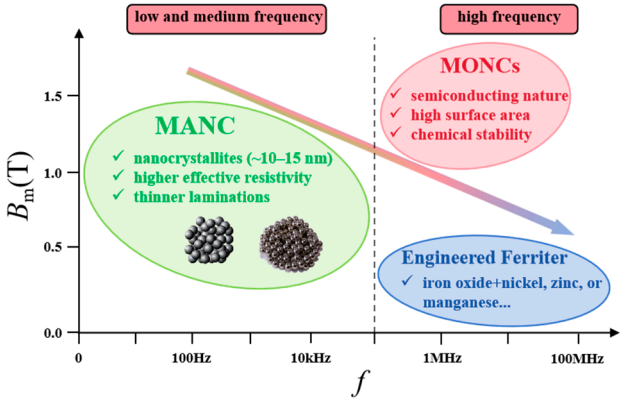


Figure 2. State-of-the-art materials for high power and high frequency applications.

Table 1 summarizes the magnetic properties of soft magnetic materials. B_s is the saturation magnetization, H_c is the coercivity, μ_{max} is the maximum permeability, R is the

electrical resistivity, λ_s is magnetization, and T_c is Curie temperature. Nanocrystalline materials, such as Fe-Si-B-Cu-Nb (FINEMET), are highlighted in the table for their unique properties. These materials exhibit low coercivity, ranging from 2–8 A/m, which is beneficial for applications requiring easy magnetization and demagnetization. The maximum permeability of FINEMET is notably high, varying from 50 to 120 $\times$ 10^3, indicating its superior magnetic responsiveness and efficiency in magnetic circuits. Overall, amorphous and nanocrystalline alloys exhibit high B_s and low coercivity, and their moderate resistivity can be additionally improved by the interface insulation. Thus, they are beneficial to use in high frequency conversions.

Table 1. Summary of magnetic properties of soft magnetic materials.

Material	B_s (T)	H_c (A/m)	μ_{max} ($\times 10^3$)	R (Ωm)	λ_s (ppm)	T_c (K)
Fe-Co-Ln-B [8]	0.84–1.66	1.0–36	8.3–12.5	-	1–58	735–850
Fe-Si-B-Cu-Nb (FINEMET) [9]	1.18–1.56	0.45–5.2	27–209.1	-	0–20	843
Fe-Si-B-P-Cu [10]	1.82–1.85	5.8–7.6	24–27	-	2.3	728
Fe-Zr-B-Cu [11]	0.70–1.60	3.2–3.5	48	-	−2–16.6	873
Permalloy ($Fe_{15}Ni_{80}Mo_5$) [3]	0.80	0.3–2	500	7×10^{-8}	1	690
$Fe_{50}Ni_{50}$ [3]	1.60	4	100	4.8×10^{-7}	25	720
Sintered Mn-Zn ferrites [3]	0.4–0.55	5–20	1–10	10^{-2}	−2	403–553

In 1967, the first amorphous soft magnetic alloys were prepared by using a rapid solidification technique to produce the Fe-C-P system alloy [12]. Since the 1980s, amorphous core transformers have been put on the market. Then, in 1988, the nanocrystalline structure with ultra-fine BCC Fe grains embedded in an amorphous matrix was achieved by specified heat treatment in the alloys with Cu addition, which was forced to dissolve during rapid quenching and facilitated nuclei formation. Afterward, FINEMET became commercialized based on the Fe-Si-B system. In the early 1990s, soft magnetic composites, known as powder cores, began to gain researchers' interest [13]. Soft magnetic composites (SMCs) are often enhanced with the incorporation of insulating materials to improve their properties; however, this process can inadvertently create air gaps that may diminish their relative permeability. Furthermore, while SMCs composed of nanoscale particles hold promise for superior performance, they have yet to be widely adopted in industrial settings. In recent years, there have been constant efforts to interpret magnetism, like the intergranular exchange effects. Intergranular exchange effects refer to the exchange coupling between adjacent grains or nanoparticles. These effects arise due to the interaction of the spins of adjacent grains, which are influenced by the boundary conditions, crystal structure, and surface states of the nanoparticles. Nogués et al. demonstrated the influence of exchange coupling in nanostructured materials, where the magnetic properties were significantly affected by the coupling between adjacent grains [14]. Similarly, grain boundary effects have been observed to modify the magnetic hysteresis and thermal stability of soft magnetic materials [15]. In addition, designs of environmentally friendly rare earth-free compositions have been studied in the past decades. To assess the environmental impact of the materials used, existing strategies include Life Cycle Assessment (LCA) and material substitution. LCA evaluates the environmental impact throughout the entire life cycle of the material, while material substitution focuses on replacing harmful or scarce resources with more sustainable alternatives.

2.2. Material Structure, Magnetism, and Correlation with Heat Treatment and Composition

Figure 3 shows the relationship between grain size and magnetic characteristics of typical soft magnetic materials. Conventional soft magnetic materials, such as permalloy,

exhibit large grain sizes, which compromise their mechanical properties, including deformation resistance. In contrast, amorphous alloys lack atomic long-range order structure, and nanocrystalline materials have small grain sizes, leading to the high ability to maintain low H_c [16]. Weak structural correlations are formed inside the materials. Therefore, amorphous nanocomposites indicate superior mechanical characteristics. For example, their yield strength can reach 3000 MPa, showcasing their exceptional strength and resilience.

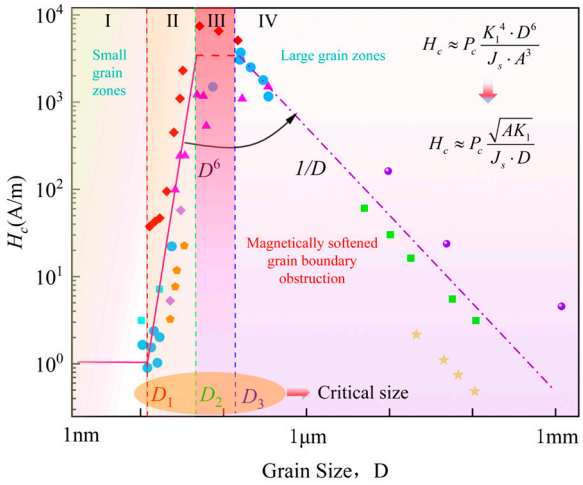


Figure 3. Coercivity vs. grain size for different soft magnetic materials: Fe-Nb-Si-B (triangle), Fe-Cu-Nb-Si-B (blue circle), Fe-Cu-V-Si-B (purple diamond and orange pentagon), Fe-Zr-B (light blue square), Fe-Co-Zr (red diamond), NiFe alloy (green square and pentagram), and Fe-6.5 wt.% Si (purple circle). Data from [16].

The increase in the coercive field with grain size can be attributed to the transition from single-domain to multi-domain states in the grains. For small grains, the magnetization reversal occurs via coherent rotation, which is dominant within a certain critical radius. This process is strongly influenced by exchange interaction, which refers to the quantum mechanical interaction between spins within a grain. The exchange interaction provides a coupling mechanism that aligns spins in adjacent atomic sites, ensuring uniform magnetization within the grain. For grains smaller than the critical radius, the exchange interaction stabilizes the single-domain state by suppressing the formation of domain walls, as the energy cost of forming a domain wall would outweigh the reduction in magnetostatic energy. It leads to a coherent reversal process with a relatively low coercive field.

As the grain size increases beyond the critical radius, the exchange interaction alone becomes insufficient to maintain a single-domain state. The increased grain size reduces the relative influence of exchange energy compared to magnetostatic energy, allowing the formation of multi-domain structures. In multi-domain grains, the magnetization reversal mechanism transitions to domain wall motion, where domain walls propagate through the material rather than through coherent rotation of all spins. This domain wall motion is also influenced by the exchange interaction at a local level, as it determines the stability and mobility of the domain walls. For instance, strong exchange coupling within grains can pin domain walls, increasing the energy barrier for their motion and consequently raising the coercive field. However, once the grains reach a size where intergranular coupling becomes weaker, the individual grains behave more independently, leading to a more pronounced multi-domain structure and a further increase in the coercive field [17].

The soft magnetic characteristics of amorphous and nanocrystalline materials can be explained by the random anisotropy model due to their small grain size D. It indicates that local anisotropies of the amorphous and nanocrystalline materials are averaged out. One of the key points of the model is the average anisotropy constant, which is the effective

first-order magnetocrystalline anisotropy constant averaged over the material, which is related to the anisotropy of the crystals and is manifested in the different energies required for magnetization along the different crystal axes, and this difference in energy is called the magnetocrystalline anisotropy energy. Magnetization is enhanced along the easiest axes and the exchange energy multiplies as A/L_{ex2}, where A is the exchange stiffness, and L_{ex2} is the length of correlation where magnetization remains constant. Actually, the microscopic system is much more complicated due to the magnetoelastic and field-induced anisotropies. It presents a decisive impact on the soft magnetic properties. It is accepted that long-range anisotropies eventually decide the minimum anisotropy inside the materials.

To obtain a thorough understanding of the thermo-magnetic properties of nanocrystalline alloys, especially for the heat treatment technique, it is vital to have an insight into intergranular exchange interaction [18]. As shown in Figure 4, the BCC grains of nanocrystalline are exchange-coupled through the intergranular amorphous matrix. When the temperature approaches Curie temperature T_c of an amorphous matrix, the domain structure becomes irregular and small. Thus, soft magnetic properties deteriorate. Meticulous alloy design must be carried out to achieve high T_c and possess a high ability of intergranular exchange coupling. By combining the properties of various structural phases, low magnetostriction could be accomplished.

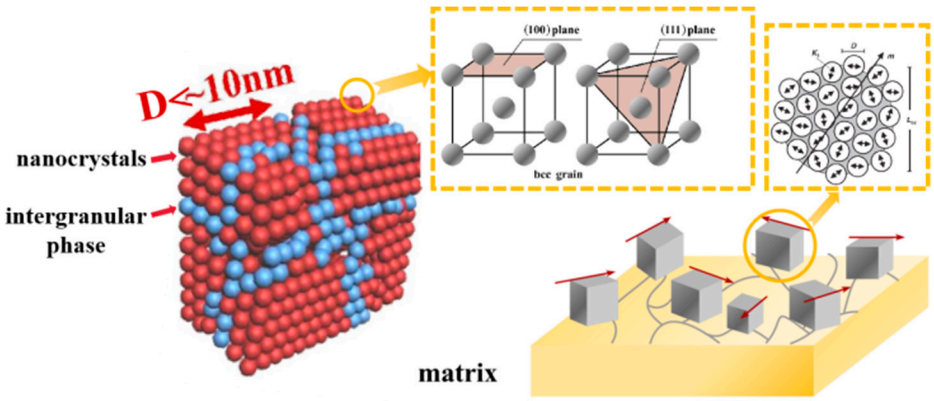


Figure 4. Schematic diagram of nanocrystalline grains (**left**) and BCC lattices with easy plane (100) and hard plane (111) (**right**).

The composition of nanocrystalline alloys has been continuously investigated. Currently, $Fe_{74}Cu_1Nb_3Si_{13-16}B_{6-9}$ behaves as an outstanding composition. Over the past decades, few attempts have been made beyond this composition. It has been reported that V can suppress the grain growth and stabilize B_s and coercivity. Mo can extend the temperature difference between the onset of α-Fe crystallization and the precipitation of the Fe-B phase [19]. Au and Cu elements can accelerate nucleation at the initial stage of crystallization. Transitional elements, including Nb, Zr, and H, restrain the increase in Fe grains [20].

Long-range nonuniformity of anisotropy is another factor that affects the magnetic properties of nanocrystalline alloys. It depends on morphology defects and inner stress. The angle between the apparent anisotropy direction and the external magnetic field determines the permeability μ. To maximize permeability, it is desirable to maximize the number of (100) planes of axes of magnetization and minimize the number of (111) planes. Meanwhile, the induced anisotropies of amorphous materials decrease steadily with the temperature. However, nanocrystalline alloys reduce induced anisotropies due to the intergranular decoupling effect.

As mentioned above, anisotropies induced by external factors determine the magnetic characteristics of amorphous and nanocrystalline alloys. The effect of field-induced

anisotropy exceeds the effects of magneto-crystalline and magnetoelastic anisotropies. Anisotropy is closely related to the size of nanocrystalline and fine structure. It can be achieved by the rapid cooling rate of melt liquid at 10^5–10^6 K·s^{-1}. Particularly, magnetic field annealing and tensile stress field annealing (i.e., tension annealing) are of great significance in obtaining uniform uniaxial anisotropy. During the magnetic field annealing process, the applied magnetic field rearranges the magnetic domain structure of the material, inducing uniaxial anisotropy along the direction of the magnetic field, thereby enhancing the magnetization ease in that direction. On the other hand, tensile stress annealing introduces stress to adjust the material's microstructure, particularly the morphology and alignment of the grains. The stress field changes the distribution of grain boundaries and affects the orientation and growth patterns of the grains. It enhances the magnetic properties of the material, particularly increasing permeability and reducing hysteresis loss due to the change in the material's anisotropy.

Stress field annealing is another promising technique to tailor the structure and anisotropy of the material. Generally, plastic deformation is induced inside the material, and uniaxial anisotropy (K_u) is linearly correlated with tensile stress. The nanocrystalline alloys exhibit a decrease in unit power losses with an increase in tensile stress. In contrast, conventional annealing without an imposed magnetic field causes an "R" shaped hysteresis loop. Induced anisotropies are consistent with the direction of spontaneous magnetization. Hence, the homogeneity of induced anisotropy by the applied field can be improved, which is beneficial to enhance the magnetic characteristics of amorphous and nanocrystalline alloys. If nanocrystalline alloys are crystallized without applied magnetic field and then field-annealed, then the K_u depends on both annealing temperature T_a and time. However, when the nanocrystallization process is accompanied by the applied magnetic field, then K_u probably remains relatively constant, regardless of the variation of T_a [21].

Figure 5 shows the effects of heat treatment on the hysteresis loops of the magnetic ring. Transverse field annealing causes a flat loop, while longitudinal field annealing contributes to a rectangular "Z" loop. A higher permeability is often desired for amorphous and nanocrystalline alloys. The rectangular hysteresis loops need to be carefully examined. It is ascribed to the dynamic magnetization behavior by the induced anisotropy. For instance, the increase in induced anisotropy enhances the expansion of domains and the localization effect, thus enlarging the anomalous losses (i.e., excessive losses) [22].

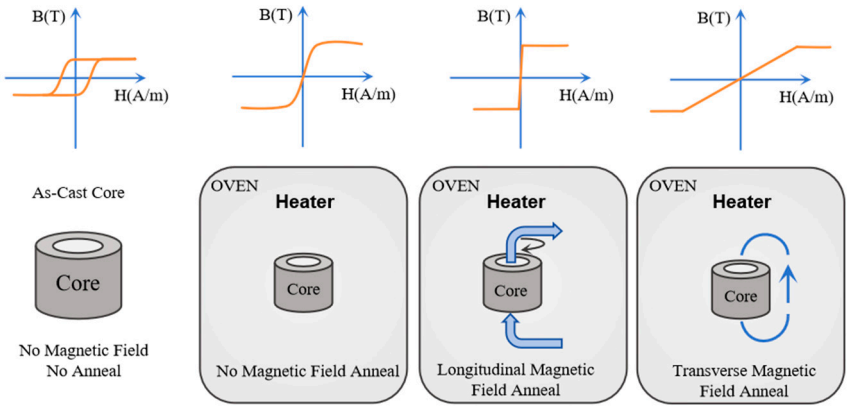


Figure 5. Hysteresis loops versus various heat treatments of soft ribbon magnetic ring.

After considering the composition and anisotropy characteristics of the material, amorphous and nanocrystalline alloys are usually fabricated into ribbons or sheets about 10–30 μm in thickness for industrial applications. The process of forming and fabricating these alloys depends on rapid cooling methods. One of the most advanced liquid phase cooling techniques is considered to be planar flow casting, which helps in achieving the

desired physical properties and dimensions of the alloys. Ensuring material uniformity and performance during the casting process is critically dependent on the optimization of key process parameters. These include controlling the cooling rate to achieve the desired microstructure, precisely regulating the casting temperature to prevent non-uniform solidification, and managing the flow characteristics of the molten metal to minimize defects. Furthermore, maintaining consistent mold temperatures and applying external pressure can enhance material uniformity and reduce internal stresses. In the actual casting process, the reservoir is in direct contact not only with the nozzle but also with the casting roll. Hence, the shape of the sheets can remain stable and reach a maximum width of 300 mm. To manufacture sheets into the desired geometry, a variety of cutting techniques can be employed, including laser cutting, chemical etching, electric discharge machining, and waterjet cutting [23,24]. Magnetic, thermal, and mechanical performances of the ribbons strongly depend on the rolled, cutting, and curing techniques. This is evidenced by the significant impact of the planar flow casting process on magnetic properties, such as permeability and losses, the critical role of high cooling rates in maintaining an amorphous structure to minimize thermal losses, and the challenges in mechanical performance due to brittleness induced during annealing, limiting the application of these materials in demanding environments [25,26].

In general, nanocrystalline alloys present superior thermal stability than amorphous alloys. Firstly, the crystal structure of nanocrystalline alloys is stable. Secondly, the duration of crystallization and field annealing of nanocrystalline is longer and more smooth than that of the amorphous material. Finally, nanocrystalline alloys could withstand severe thermal aging conditions with little fluctuation in μ. Meanwhile, nanocrystalline alloys can reach higher saturation magnetization B_s. In addition, the major compositions, such as Fe and Si, are relatively cheap. However, nanocrystalline alloys inevitably become brittle during crystallization because of the structural relaxation and the deposition of α-Fe. It limits the shape annealing of power cores. Moreover, the stress relief treatment required for high μ amorphous alloys also enhances the embrittlement. These challenges underscore the need for further research to optimize the balance between magnetic properties and mechanical characteristics in nanocrystalline alloys.

3. Application in High-Power-Density Transformers

A high-power-density transformer is an essential part of the power system. Statistically, 10 kV and 35 kV distribution transformers account for 40–50% of total power loss in China [27]. Nowadays, the development of transformers is growing toward enhanced stability, energy conservation, compactness, high power density, and controllability [28]. In recent years, power electronic transformers (PETs) or solid-state transformers (SSTs) have been competitive candidates for the establishment of flexible AC/DC power transmission, smart grid, microgrid, and renewable energy connections such as solar photovoltaic systems [29,30]. By 2010, an overall capacity of 70 million kVA and 35 million kVA of amorphous core transformers had been constructed. Table 2 presents the research findings and performance of various existing materials in high-power-density transformers.

Table 2. Comparison and improvement of different high-power-density transformers.

Type	Material	Properties	Power	Merits	Demerits
Nanocrystalline alloys [31]	Fe-Si-B-Cu-Nb (FINEMET)	B_s = 0.6–2 T; H_c = 0.5–1.0 A/m; core loss: 10^4 kW/m^3 at 100 kHz, 1.0 T	Up to 1 MW	High permeability, low losses, and low magnetostriction	Brittle; high cost
Mn-Zn doft ferrites [32]	Mn-Zn	B_s = 0.2–0.5 T; core loss: 50 kW/m^3 at 100 kHz, 0.1 T; low resistivity (0.1–20 Ωm)	-	Excellent low-frequency performance; low core loss	Low B_s; low T_c; brittle; stress sensitivity
Iron–silicon alloys [33]	Fe-Si	B_s = 1.96–2.12 T; high Curie temp ($T_c \approx$ 1030 K); low resistivity	-	Moderate cost; good thermal stability; excellent mechanical properties	Low-frequency restrictions; limited availability; brittle
Composite magnetic materials [33]	Soft magnetic composites (SMCs)	B_s = 0.7–1.0 T; H_c = 10–30 A/m; high resistivity	Up to 1 MW	Low noise characteristics; low eddy current losses; good thermal stability	Moderate permeability; higher iron loss and lower relative permeability
Amorphous/ nanocrystalline hybrids [32]	Fe-B-Si-C with Nb addition	B_s = 1.2–1.4 T; H_c = 5–10 A/m; improved Curie temp (T_c = 600 K)	Up to 1.5 MW	Low coercivity; high permeability; low loss across wide frequencies	Complex manufacturing processes

3.1. Requirement and Utilization of Soft Magnetic Materials in Transformers

Generally, Faraday's law of inductance can be used to determine the relationship between the voltage and the current of a magnetic core inductance L. If the excitation current of the winding is a sinusoidal waveform, the voltage of an ideal toroidal core with inductance L can be depicted by the following:

$$V = \frac{-\mu N^2 A}{l} I_0 \omega cos\ (\omega t) \quad (1)$$

If V, μ, N, and L are constants, then the cross-sectional area A is negatively correlated with frequency f ($\omega = 2\pi f$) [34]. Thus, an increase in frequency can significantly reduce the size of the magnetic components, thereby cutting down the overall size and weight of power converters. Furthermore, the power density would increase, resulting in the improvement of the power conversion flexibility.

Nevertheless, the compaction of soft magnetic cores with limited size restricts heat-dissipating (limited space for high-power windings). Therefore, soft magnetic materials with superior characteristics, including magnetic parameters, mechanical properties, and thermal behaviors, are required for high-power and high-frequency applications. Table 3 shows the characteristics of soft magnetic materials for high-power electronic applications.

Table 3. Desired soft magnetic characteristics of materials.

Characteristics	Explanation
Broadband capability	Fit in with PWM excitations with multi-frequency components
Higher B_s	Enhance the efficiency of power converters
Appropriate μ in driving field direction	Reduce static hysteresis loss
High R with high thermal conductivity ρ	Reduce high eddy current loss

3.2. Transformer Cores

3.2.1. Amorphous and Nanocrystalline Alloy Core Materials

Since the first commercial amorphous material (the Metglas) was manufactured, there are three fundamental types of amorphous materials, including Fe-based, Co-based, and Ni-based materials [35]. Iron-based materials are most commonly used. The high cost of cobalt restricts the application of Co-based material. Table 4 shows the comparison of the electromagnetic properties of amorphous core materials. Metglas is the world's first commercialized soft magnetic amorphous material, introduced by Hitachi Metals Ltd. in Tokyo, Japan. VITROVAC materials are manufactured by VACUUMSCHMELZE (VAC), headquartered in Hanau, Germany. Apart from the amorphous material, the nanocrystalline materials with excellent magnetic characteristics, such as high B_s, high μ, and high T_c, exhibit superior performance in high-frequency and high-power fields. Table 5 shows the comparison of nanocrystalline materials with conventional materials. It should be noted that the nanocrystalline alloys with a high $B_s \geq 1.7$ T cannot be scalably produced and commercialized up to now because of their poor amorphous formability for wide ribbon production, fast heating rate requirement for grain refinement, and narrow parameter window for uniform annealing for large cores. Additionally, it is believed that such dilemmas cannot be overcome in the near future, stressing the need to explore revolutionary strategies.

Table 4. Comparison of amorphous materials utilized in transformers.

Magnetic Materials	Substrate	B_s (T)	Core Loss/0.3 T, 100 kHz (W/kg)	Resistivity (μΩ·cm)	ρ (g/cm^3)
Metglas 2714A [35]	Co	0.57	120	1.38	7.90
Metglas 2705M [35]	Co	0.77	260	1.42	7.59
Metglas 2826MB [35]	Ni	0.88	1360	1.38	7.90
Metglas 2605S3A [35]	Fe	1.41	300	1.38	7.29
Metglas 2605SA1 [35]	Fe	1.56	1400	1.30	7.18
VITROVAC 6025F [36]	Co	0.40	100	1.40	7.8
VITROVAC 6030F [36]	Co	0.70	110	1.30	7.75
VITROVAC 6155F [36]	Co	0.90	130	1.10	7.90

Table 5. Comparison of nanocrystalline materials with conventional materials.

Magnetic Materials	B_s (T)	P10/1	P3/10	P2/10	P2/100	Ω	ρ	H_c
0.6 wt% Si-steel [37]	1.80	18.1	30	-	-	-	-	-
Grain oriented Si-steel [37]	2.03	27.1	-	-	-	-	-	-
Fe-Cu-Mo-Si-B alloy [38]	1.75	5	-	8	40	-	-	-
Fe-Si-B-Cu alloy [39]	1.85	-	-	-	-	-	0.7	6.5
Fe-Si-B-P-Cu alloy [40]	1.76–1.94	-	-	-	-	-	-	5–10
VITROPERM [35]	1.20	-	1.5	-	40	1.15	7.35	-
FINEMET [35]	1.23	-	5	-	80	1.20	7.30	-

P10/1 represents the core losses at 1 T and 1 kHz, P3/10 represents the core losses at 0.3 T and 10 kHz, P2/10 represents the core losses at 0.2 T and 10 kHz, and P2/100 represents the core losses at 0.2 T and 100 kHz, all with the unit W/kg. The unit of ρ is g/cm^3, and the unit of H_c is A·m^{-1}.

Nanocrystalline material presents similar resistivity with amorphous alloy, while it indicates a much lower core loss. Co-based Metglas 2714A, Metglas 2705M, and VITROVAC 6025F to 6155F exhibit improved core loss properties. However, the low Bs restricts its applications in high-power-density fields.

The key aspects of transformer core design include surface treatment, heat treatment, lamination, manufacture solidification, core shaping, and air gaps (cutting). In the case of transformers used in the frequency range of kHz, toroidal, type CC, and shell type are fundamental shapes. There are relevant experimental results showing that toroidal cores have the highest efficiency and lowest cost, and the CC type has a high output power range [41]. Currently, toroidal cores were used in the earliest transformers. Then, cutting techniques for amorphous ribbons enable the accomplishment of low core loss by the design of distributed-lap joint connected cores. However, distributed-lap joint wound cores for HFT based on amorphous alloys have been barely commercially fabricated. Firstly, the fabrication of thin film amorphous ribbons is difficult. Secondly, it is challenging to handle the embrittlement of amorphous ribbons after annealing [42].

One solution is a mixed method combining consolidating and hot-cutting techniques. The method utilized consolidation to reduce manufacturing time and hot cutting (e.g., laser cutting) to maintain the magnetic properties of stacked cores. Another solution is a two-stage heat treatment process in which a toroidal core is rapidly heated at more than 1000 K/s and rapidly cooled at more than −1000 K/s. This is a two-stage heat treatment process in which a toroidal core is rapidly heated at more than −1000 K/s and rapidly cooled at more than −1000 K/s [43,44]. It prevents the deterioration of ductility of amorphous ribbons compared with the as-quenched state. Glue, such as polyester, is a determining factor of stacking factor S = m/(V·ρ) during the consolidating process, which is superior to polyethylene. The results of the study on the effect of different joint types of stacked cores on core losses show that the efficiency of step-lap stacked cores is higher than that of non-step-lap stacked cores and distributed-lap wound cores, where it was also demonstrated that $1/\mu_r$ is positively correlated with the increase in air gap length [45]. When the permeability of the core material is high, the introduction of an air gap avoids saturation magnetization and reduces the remanent magnetization Br but increases the leakage inductance and power loss [46]. There are two typical types of air gaps, i.e., concentrated and distributed gaps, as shown in Figure 6. The latter are distinguished from concentrated air gaps in that their air gaps are divided into several parts to mitigate fringing flux. Nevertheless, it increases the manufacturing cost. Therefore, it is necessary to design the proper air gap size and configuration technique.

To enhance the magnetic properties of materials when subjected to high-frequency excitation, advanced surface treatments are integrated into the manufacturing process. These treatments encompass techniques such as deposition and plasma spraying, which are designed to modify the material's surface properties, thereby optimizing its performance in high-frequency applications. Generally, oxides, nitrides, or fluorides serve as coating or film layers. Ferrite and iron layers prepared through electrochemical methods exhibit excellent magnetic properties [47]. ZrO addition is proven to reduce core loss and improve quality factor $Q = \omega L_{eq}/R_{eq}$ [48]. The reactive sputtering technique produces higher induced anisotropy and B_s [49,50]. In particular, recent studies have demonstrated that controlled sputtering conditions, such as those involving tandem-sputtering methods, can further optimize magnetic properties by fine-tuning the nanostructure and anisotropy field, leading

to enhanced performance in high-frequency applications [51]. A nanocrystalline flake ribbon (NFR) was developed recently by indicating a lower P_c, higher B_s, and temperature stability than ferrite N87 and N27 [52]. It presents potential applications in high-power-density magnetic cores.

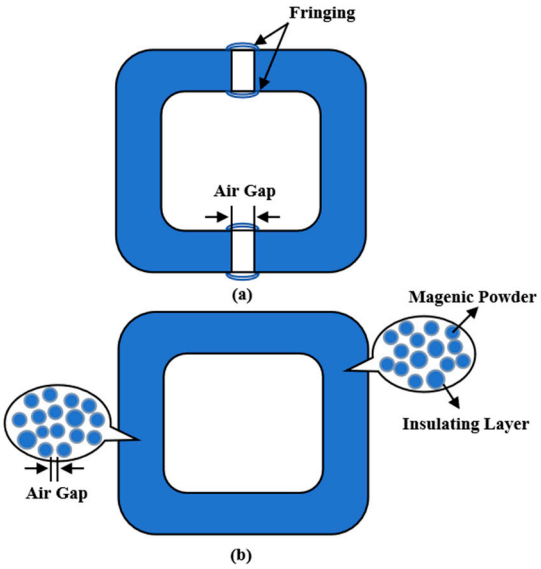


Figure 6. Magnetic core with (**a**) concentrated air gaps and (**b**) distributed air gaps.

3.2.2. Principle and Calculation of Magnetic Core Power Loss

The power loss model of sinusoidal voltage is primarily derived from Bertotti's theory [53]. In general, the core loss can be divided into three components, including eddy current losses P_e, hysteresis losses P_h, and excess losses (i.e., anonymous losses) Pex. Pex strongly depends on the domain wall structure, especially for the particle boundary inside the material. The total core loss can be expressed as follows:

$$\begin{aligned} P &= P_h + P_e + P_{ex} \\ &= K_h f B_s^2 + \frac{\sigma d^2}{12\rho T}\int_0^T \left|\frac{dB(t)}{dt}\right|^2 dt + \sqrt{\sigma G S V_0}\frac{1}{T}\int_0^T \left|\frac{dB(t)}{dt}\right|^{1.5} dt \end{aligned} \quad (2)$$

where B_s is the peak magnetization, f is the frequency of voltage, ρ is the resistivity of material, d is the thickness of lamination, S is the cross-sectional area of the lamination, T is the cycle of magnetization, and G is constant. V_0 is the internal statistic coefficient [54].

Classical eddy current loss originates from magnetic domain wall motion, which is described as Equation (3). d is the thickness of the material, and ρ is the resistivity. The equation is available when $d \ll \sigma$. In this case, skin effect can be reasonably ignored. It indicates that the eddy current loss increases significantly as frequency increases.

$$P_e = \frac{\pi d^2 B_s^2 f^2}{6\rho} \quad (3)$$

Generally, it is necessary to use the theoretical models for core loss evaluation. Preisach, Jiles–Atherton (J-A), and Stoner–Wolhfarth (SW) models were generally used to calculate the Pex. In the Preisach model, the magnetic material is decomposed into several magnetic dipole units. The calculation of the hysteresis loop can be improved by a finite element algorithm with variable temperature [55]. In the classical J-A model, Man is the anhysteretic magnetization, which is given by Equation (4).

$$M_{an} = M_s[coth(H_e/a) - aH_e] \quad (4)$$

where H_e is the Weiss' effective field and is $H + \alpha M$, M_s is the saturation magnetization, k is the hysteresis loss coefficient, α is the domain coupling, and c and a are parameters depending on reversibility and shape. Subsequent modified models consider the temperature, magnetoelastic effect, magnetomechanics, anisotropy, frequency, and stress dependence [56–58].

The SW model was employed when it represents single-domain ellipsoidal particles, as shown in Table 6, where W is the total energy of single-domain particles, Keff is the structure and anisotropy of the particle, θ is the angle between magnetic torque and easy axis, and ψ is the angle between the external magnetic field and easy magnetization axis [58]. However, the approach has limitations in its ability to dynamically model the behavior of soft magnetic materials with flexibility. The process is also cumbersome and time-intensive, as it relies on the iterative solution of the static magnetic energy minimization equation to progress. In addition, researchers found that the orientation of domain walls significantly changes the structure's non-uniformity [59]. This can be modified by Pry and Bean's model, which considers the dynamics of domain wall motion of the materials [60].

Table 6. Models of hysteresis loss calculation.

Model	Equation	Pros	Cons
Preisach classical form [61]	$B(t) = \iint \mu(\alpha,\beta)\gamma(\alpha,\beta,H(t))d\alpha d\beta$	Intuitive accurate	× Edomain
Preisach vector form [62]	$B(t) = \int_{-\pi 2}^{\pi 2} \rho(\theta)d\theta \iint \mu(\alpha,\beta)\gamma(\alpha\beta H(t))d\alpha d\beta$	Angular dispersion flexible	
SW classical form [63]	$W(\theta,\psi) = \frac{1}{2}K_{eff}cos^2\theta + K_{eff}cos^4\theta + K_{eff}sin^4\theta$	Anisotropy specified	× soft magnets
JA classical form [64]	$dM/dH = \frac{\delta_M(M_{an}-M)+k\delta cdM_{an}/H_e}{K\delta-\alpha[\delta_M(M_{an}-M)+k\delta cdM_{an}/H_e]}$	Less parameters	× Edomain × anisotropy

Bertotti's model is modified to evaluate the core losses under square wave and delta voltage excitation. The key issue of Bertotti's analytical model is the unknown parameters, which are difficult to extract. Hence, it is time-consuming and inconvenient to use in design applications. In contrast, Steinmetz's empirical method predicts sinusoidal-excited loss in a more concise way. The key weakness of the original Steinmetz model is the mismatch between the assumption of sinusoidal excitations and the actual PWM excitation. Numerous studies have investigated the effects of harmonic effects, flux density variations and their instantaneous or peak-to-peak values, or the effect of the usage factor KFWC, which corresponds to the ratio of the non-sinusoidal to the sinusoidal area of a typical waveform [65–70]. These models are correspondingly modified Steinmetz expression (MSE), generalized Steinmetz expression (GSE), improved generalized Steinmetz expression (IGSE), natural Steinmetz extension (NSE), equivalent elliptical loop (EEL), and waveform coefficient Steinmetz equation (WcSE). Figure 7 shows the comparison results of the aforementioned method. Different models exhibit distinct rates of change in magnetic induction. WcSE predicts that core losses are lower than those predicted by any other models. However, as the zero voltage period increases, the modified models, including WcSE, start to exhibit core losses that are 1.2–1.3 times higher than OSE [71].

Researchers improved these models by considering the relaxation time during zero voltage despite the extensive calculations and multiple parameters [72]. The impact of duty cycle and frequency was considered [73]. Figure 8 illustrates the estimation results, which are in agreement with the measured power loss. Transverse anisotropy Mn-Zn ferrite samples have been measured at B_p = 100 mT up to about 1 MHz. It shows the analysis of the magnetic loss behavior of the Mn-Zn ferrite. In addition to measuring the loss under triangularly symmetric induction of $W_{TRI05}(f)$, the loss under asymmetric induction ($W_{TRI02}(f)$) with duty cycle α = 0.2 and asymmetric induction ($W_{TRI01}(f)$) with α = 0.1 (symbols) was measured, and the loss decomposition of sinusoidally induced $W_{SIN}(f)$ was performed

to obtain the loss components and predicted and then compared with the experimental results of $W_{TRI05}(f)$, $W_{TRI02}(f)$, and $W_{TRI01}(f)$. $W_{rot,SIN}(f)$, a simplifying and relatively crude approximation for the Mn-Zn ferrite, where the slope of the predicted $W_{rot,SIN}(f)$ undergoes a rapid change around 1–2 MHz [74]. However, the effects of manufacturing-related factors, such as strong and un-uniform external stress, solidification, surface treatment, servicing temperature, etc., on the core loss have not yet been conducted. The method to analyze and calculate the corresponding proportion remains unknown. Additionally, since there are strong size effects on the magnetic properties of the cores, it is also challenging to verify the simulated results.

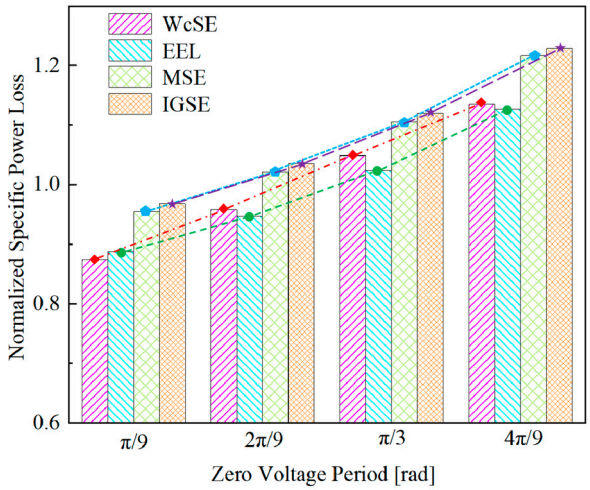


Figure 7. Core loss model comparison for Metglas POWERLITE C-cores, with $\alpha = 1.51$, $\beta = 1.74$, and $K = 6.5$; therefore, $k_i = 0.62$, $C_{\alpha\beta} = 8.45$, and $C_{\beta\alpha} = 7.04$ for a waveform with $f = 1$ kHz and $B_{sq} = 450$ mT. Theoretical results are normalized to OSE. Data from [71].

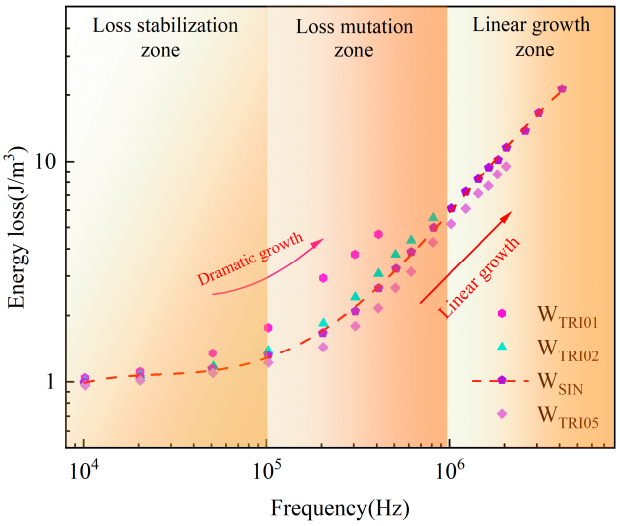


Figure 8. Magnetic loss behavior of Mn-Zn ferrites. Data from [74].

3.2.3. Thermal Simulation and Modeling

Accurate prediction of temperature distribution of transformers benefits for failure diagnosis, as well as design optimization and testing. Finite element method (FEM), computer fluid dynamics (CFD), and thermal network modeling are most preferred by researchers [75]. CFD is more discretized, making it both more flexible and demanding in terms of computing power. Moreover, the CFD method ignores the effects of turn insulation. In contrast, Thermal network models can run faster and are more commonly used [76]. Basic

components of dry-type transformers can be regarded as nodes in the thermal network. The parameters of the thermal network can be described by Equations (5)–(8).

$$d_e = P_i / P_e \tag{5}$$

$$R_{cond} = \frac{1}{2\pi\lambda} ln \frac{r_1}{r_2} \tag{6}$$

$$R_{conv} = \frac{1}{hA} \tag{7}$$

$$q_{rad} = \frac{\sigma_b \left(T_1^4 - T_2^4\right)}{1/\varepsilon_1 + ((1-\varepsilon_1)/\varepsilon_2) r_1/r_2} \tag{8}$$

where d_e is the proportion of eddy current loss, R_{cond} and R_{conv} are thermal conduction and convention resistances, respectively, λ is the thermal conductivity, r_1 and r_2 are the inner and outer radius of windings simplified as a cylinder, h is the surface heat transfer coefficient, σ_b is the Stefan–Boltzmann's constant, T_1 and T_2 are absolute temperatures of two radiating surfaces, and ε_1 and ε_2 are emissivity of surfaces, respectively.

A thermal model applied to the foil windings of a ventilated dry-type power transformer with a rating of 2000 kVA has been proposed, and the temperature distribution has been determined by the Finite Element Method (FEM), followed by experimental temperature measurements with thermocouples and used to validate the FEM results [77]. A genetic algorithm was applied to realize diameter optimization of cooling ducts and coils by the CFD-based model [78]. A quasi-3D coupled-field method was proposed to study temperature rise in ventilated transformer windings [79]. Artificial neural networks were used to analyze winding temperature [80]. Researchers managed to couple FEM and CFD methods by thermal network to sort out thermal parameters. It presents more appealing precision than the empirical formula [81]. Results of the 3D coupled magneto-fluid-thermal model free of empirical h agree with the testing results of hot-spot temperature [82]. A particle filter optimization approach with support vector regression was used to predict the hot spot temperature of SST [83].

3.2.4. Insulation and Vibration

Transformers operating under high-frequency electric stress with high power are subjected to high frequency, high voltage, and heating. This necessitates a special insulation design. To be specific, a qualified design should pass three dielectric tests: lightning impulse test, voltage withstand test, and partial discharge evaluation [84]. The insulation of HFT consists of main insulation, inter-turn insulation, and inter-layer insulation. The primary insulation is situated between windings of varying voltage levels, as well as between the lead wire and magnetic core, in addition to the ground.

$$\frac{D_s}{D_{sref}} = \left(\frac{T_{ref}}{T}\right)^{0.4} \tag{9}$$

where T_{ref} and D_{sref} are the thickness and dielectric strength of the reference material, respectively. Thus, the choice of insulation materials, along with the investigation of insulation design, lays the foundation for a successful transformer construction. It should be noted that additional attentions should be paid to the viscosity, infiltrations, shrinkage coefficient, etc., of the dielectric materials, which has a strong influence on the uniformity of insulation layer and the magnetic properties of the core.

Acoustic noise is generated by the complicated vibration of transformers. It originates from electromagnetic excitations, such as the magnetostriction λ the Maxwell force of the core, and the Lorentz force of the windings. The λ_s is different for different winding

topologies, e.g., λ_s is 27 μm/m for Fe-based Metglas 2605SA1 and <0.2 μm/m for Co-based VITROVAC 6030 [85]. It is worth noting that the noise level strongly depends on the annealing process and external stress of the core, and the real magnetostriction deviates from the documented λ_s largely. Experimental results indicated that the transformer tank vibration can increase the average sound pressure level by 28 dB [86].

Magnetostriction is considered the primary cause of loss due to core vibration, which is depicted by $\Delta l/l$, where l is the material length, and Δl is the difference of l [87,88]. Joule magnetostriction is primarily associated with core vibration, where λ is described as a function of H and mechanical stress σ. The Maxwell force mainly occurs at the joints of laminated cores and between layers [89]. Furthermore, the Maxwell force interacts with magnetostriction to contribute to the vibrational behavior of soft magnetic materials, especially noticeable in cut cores that incorporate air gaps, leading to significant vibrational amplitudes. In comparative terms, the vibration and noise levels of transformer cores made from Co-based amorphous alloys are found to be lower than those of their Fe-based counterparts. Notably, transformer cores fabricated from nanocrystalline alloys demonstrate reduced noise emissions, making them a favorable choice for high-frequency transformer (HFT) designs, where acoustic signature is a critical consideration.

Conventional transformer design is basically a draining procedure of revising existing ones based on the rule of thumbs. It has limited variables due to the excessive development cycle. With the rise of artificial intelligence and smart software platforms, achieving a more efficient and comprehensive design has become a realistic possibility. Currently, finite element analysis is the most popular due to its flexibility and efficiency. Various parameters, such as temperature rise, leakage inductance, and insulation, as well as frequency, voltage, current, and turns ratio, are needed to be optimized. Typically, the optimization algorithm takes into account factors such as ambient temperature, winding turns, wire gauge, core size, winding structure, and insulation materials as input. Artificial neural network (ANN) has been applied to develop a design platform for coaxial transformers [90]. Unlike other MFT design procedures, there is a new design methodology that uses a modified version of the area-product technique, which includes a clever modification of the core loss calculation, where nanocrystalline cores are used. The core loss is calculated by a full analysis of the dispersive inductance, and finally, for validation, the MFT model connected to the DAB converter is simulated in Matlab-Simulink (The MathWorks, Tokyo, Japan, v2014a) [91].

Progress can also be found in the novel insulation design of high-frequency DC-DC converter and MFT design. Recently, a new insulation and cooling structure has been proposed for 100 kW parallel concentrically wound MFTs, and for the first time, a 3D-printed winding with heat sinks has been demonstrated. Regarding recent research on high-power MFT prototypes, a representative report on MFT design in 2021 shows that at 15 kHz, rated at 200 kW, the material is nanocrystalline, the cooling method is air-cooled, the insulation voltage is 5.3 kV in partial discharge insulation tests, the efficiency is 99.84%, and the power density is 19.23 kW/cm^3 [92].

Design optimization of the power core minimizes the eddy current losses and mechanical vibrations, which are caused by magnetostriction correction models, such as the Steinmetz Method of Experiences (MSE). It can estimate the losses in non-sinusoidal waveforms, such as the PWM waveform. In addition, strategies such as specializing in insulation configurations, enhancing thermal management, and addressing complex electro-thermal–mechanical field coupling effects can promote the development of high-power-density transformers with better performance.

4. Application in Power Inductors

4.1. Requirement and Utilization of Soft Magnetic Materials in Inductors

Soft magnetic materials can be used in the magnetic cores of high-power inductors. The requirements of magnetic materials of inductors, such as amorphous and nanocrystalline alloys, are similar to power transformers. The performance of inductors can be assessed by the quality factor Q, which is defined by the equation $Q = E_{stored}/E_{lost}$. To maintain excellent performance in the working frequency range of kHz and above, high μ, mechanical strength, and packing density, low power loss and vibration, and excellent DC bias properties are required for high-power inductors. One of the main distinctions between inductor and transformer cores lies in their respective functions. Inductors can be used as temporary energy storage devices, while transformers are power–magnitude conversion devices [93]. Therefore, although high permeability remains desirable for inductors, it is not as rigorously essential as it is for transformers. Therefore, a wider range of magnetic materials can be used for inductors.

Nanocrystalline powder cores, using soft magnetic composites (SMCs), have been a heated research topic over the past two decades and generally have greater diversity. The flexibility of adjustment in terms of powder size, ingredient proportion, dielectric additives, and stress and field treatment contributes significantly to the versatility of this approach. Comparison between nanocrystalline powder cores and conventional powder cores reveals that the former exhibits superior loss reduction in higher frequency ranges, such as 450 kHz and above [94]. The development of novel materials exhibiting exceptional performance has been achieved for the purpose of inductor applications. Researchers developed a powder core with a maximum μ of 35.5 and power loss of 562.2 mW/cm^3 at 1 MHz by mixing amorphous Fe alloy and sub-micro α-Fe by 7:3 [95]. A recent study has investigated a material with low-cost magnetic material properties for making cores for resonant converter inductors. The material consists of an unsaturated polyester mineralized resin, COR61-AA-531EX, and a 200-mesh iron powder with a particle size of 74 microns and has the magnetic properties of a "soft magnetic composite" with good magnetic properties in high-frequency and high-stress applications [96].

4.2. Configuration of Inductor Cores

In terms of the geometry of powder cores utilized by soft magnetic materials, there are several typical types of cores, including nanocrystalline magnetic block cores (NMBCs), nanocrystalline magnetic stacked cores (NMSCs), toroidal cores, and planar cores [97]. Toroidal cores consisting of Fe-Cu-Al-Si-B exhibit appealing denoising characteristics. They are usually made up of laminated ribbons 14–22 μm in thickness. The width of air gaps has been reported as the most influential factor on the inductance L and tunability [98]. In general, two types of air gaps in toroid cores can be prepared, such as the distributed air gap and the concentrated air gap. The latter can reduce the overall μ of the core and, thus, improve magnetization saturation. Nevertheless, it is hard to handle the issue of edge flux generated out of concentrated air gaps. In view of that, the distributed air gaps with insulation materials between the laminations are introduced in the cores to reduce the size of air gaps. However, toroid cores have a weight limit of a few kilograms per core, rendering them unsuitable for larger power conversion systems. In contrast, nanocrystalline magnetic stacked chips (NMSCs) and block cores (NMBCs) can be fabricated to large sizes and weights, as shown in Figure 9, and are mainly used in power electronic devices requiring high core mass and magnetizing current frequencies in the 1–30 kHz range [99]. They can also maintain a low power consumption of 2 w/kg at 10 kHz and 0.1 T. Different construction methods for NMSCs and NMBCs are illustrated in the figure, and their common feature is that they offer design choices for a variety of parameters, such as the

number of laminations, the air gap width, and the configuration of the laminations or blocks, so that the core design can be optimized for practical applications.

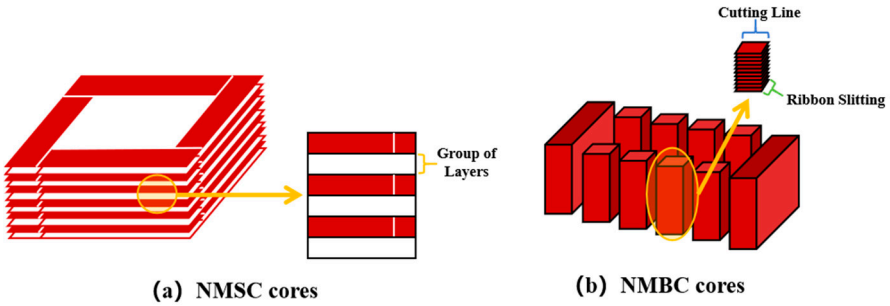


Figure 9. Construction of inductor cores: (**a**) NMSC; (**b**) NMBC.

Furthermore, new types of configurations have been conducted for high-power inductor core design. A single-layer core targeting 3–30 MHz frequency with quasi-distributed gaps based on pot cores was designed. It can achieve a quality factor of 980 [100]. A constructed concentric dual core for common mode inductors can lead to a significant reduction in near-field interference. A novel planar inductor configuration characterized by orthogonally distributed air gaps and with low AC winding losses has been proposed for an 8 kW, 250 kHz buck converter.

4.3. Application in Inductor Cores

Potential applications for nanocrystalline alloy inductors are to build energy conversion elements, such as solid-state buck-converters, high-frequency chokes, wireless power transfer, and voltage tunable inductors. Table 7 shows a brief comparison of the application in different power converters.

Table 7. Comparison and improvement of different inductor cores.

Type	Composition	u_r	P (mW/cm^3) at 0.1 T and 100 kHz	B_s	T_c (°C)	P_h Dependence of f at B_p = 0.1 T
Sendust [101]	Fe-Al-Si	100	900	1.0	500	1.07×10^{-4}
Kool Mμ [94]	Fe-Al-Si	14–125	-	1.0	500	-
Molypermalloy [101]	Ni-Fe	100	700	0.6–1.0	410	2.76×10^{-5}
High Flux [94]	Fe-Ni	14–160	-	1.5	500	-
MPP [94]	Fe-Ni-Mo	14–550	-	0.8	460	-
XFlux [94]	Fe-Si	26–90	-	1.6	700	-
Mega Flux [94]	Fe-Si	26–90	-	1.6	700	-

4.4. Design and Manufacturing of Power Inductor

4.4.1. Winding Design of Inductors

Similar to the power transformers, the winding design follows the loss evaluation, configuration, parasitic parameters, etc. The first determining factor is manufacturing flexibility. For lower AC resistance and high-frequency applications, both Litz wire and copper foil are popular candidates. However, Litz wire is no longer suitable because of its manufacturing inflexibility. Secondly, to reduce the power loss of inductors, much attention must be given to achieving an evenly distributed magnetic field strength H across the magnetic component. An auxiliary magnetic path can be regarded as a shunt with low μ to reduce fringing flux [102]. For example, a cutting core can be introduced in the original structure. In addition, foils are chosen to reduce the proximity effect of the windings [103]. Thirdly, when inductors are operating under a high dv/dt electric stress, the interwinding capacitance is a type of parasitic parameter that is necessary for reduction. It can be

realized by increasing the number of layers and applying thicker spacers [104]. Finally, the inductor should be able to resist external magnetic fields. Equivalent current loops and circuits have also been derived to illustrate the generation and elimination of induced noise voltages in inductors with various winding configurations, where the direction of the inductor input line end is defined as the x-direction, the direction of the inductor side is defined as the y-direction, and the z-direction is defined as perpendicular to the plane of the inductor [105].

4.4.2. Vibration and Noise

The noise and vibration of inductors are driven by Maxwell force, Laplace force, and magnetostriction, which are constantly distorting the inductor cores and threatening the reliability of inductors [106]. If the permeability of the core is a constant, the total deflection of the yoke can be depicted as follows:

$$\Delta x = \lambda_T(B)(n-1)l_c - n\frac{B^2 e}{2\mu_0 E} \tag{10}$$

where e is the thickness of air gaps, E is the Young modulus of the air gap, λ_T is magnetostrictive coefficient, and B is the ideal no-fringing field. According to the quasi-state equation, it is sensible to select materials with higher λ_T, like ceramic. In the future, a delicate balance between λ_T, E, and pre-stress level may achieve opposite phases of Maxwell force and magnetostriction, thereby canceling the distorting effect.

The addition of silicon rubber cushion and foam bindings can lessen the level of acoustic noise of the amorphous alloy cores [107]. Various core geometries, including oval, toroidal, and rectangular shapes, and magnetic materials, including HighFlux, MegaFlux, and Sendust, were investigated [108]. The vibration and acoustic noise behaviors were studied and compared.

Electromagnetic interference (EMI) filtering chokes are essential components in power electronics systems to suppress conducted and radiated electromagnetic noise. These chokes are primarily designed to mitigate common-mode and differential-mode noise, ensuring the electromagnetic compatibility (EMC) of power systems. By introducing inductance into the circuit, EMI chokes impede the high-frequency noise currents while allowing low-frequency power currents to pass through with low loss.

Distributed parameter circuit models can be used to provide insight into the internal physical properties of EMI filter chokes, which is useful for the initial design of chokes [109]. The distributed parameter circuit model of an EMI filtering choke usually consists of a single RLC parameter per turn, which usually has a well-defined physical meaning. Kovacic et al. [110] obtained these RLC parameters through analytical calculations. In addition, M.C. Caponet et al. demonstrated a five-step design procedure for the design of EMI filters for power electronic equipment: (1) measure the noise impedance; (2) determine the sink impedance; (3) measure the noise spectrum (both common and differential components) over a standardized bandwidth and check for the predominance of certain components; (4) set the required attenuation of the selected mode at a specific frequency; (5) select the filter topology and calculate the values of the components that satisfy a given limit curve. This design procedure and the understanding of the noise components make the design of filters easier and more optimized [111].

5. Application in Power Motor

Amorphous alloys have been applied for mature industrial use like aircraft power plants [112–114], and the amorphous alloys were utilized in the stator teeth structure [115]. A motor with an amorphous stator core was developed in 1981 [116]. Application of

amorphous cores can reduce motor power loss by 70% [117]. A high-speed amorphous reluctance motor was designed, and its core loss was only one-fifth of silicon steel motors at 48,000 rpm [117]. The amorphous alloy was utilized to fabricate a brushless permanent DC motor [118]. In 2005, an axial flux permanent magnetic motor was built by [119] with amorphous cut cores, yielding high power density. An axial gap motor with an amorphous core to conserve space was manufactured [120]. In 2021, an amorphous inductor motor was built by [121] to secure the mechanical strength of the rotor during operation. Lately, there has been a rise in the development of electric motors that use less expensive rare earth materials or even designs that eliminate the need for rare earth altogether. Depending on the rotational speed, they can generate sufficient torque and maintain a stable output voltage.

Table 8 presents the research findings and performance of various existing materials in power motor applications. The table provides a detailed comparison of material types, properties, and power ratings, as well as their merits and demerits.

Table 8. Comparison and improvement of different power motors [122,123].

Type	Material	Properties	Power Rate	Merits	Demerits
Nanocrystalline Alloys	Fe-Si-B-Cu-Nb (FINEMET)	B_s = 1.25–1.30 T; H_c = 2–8 A/m; Low core loss	Up to 100 kW	Low core loss; High permeability	Brittleness; Limited thermal stability
Amorphous Alloys	Fe-B-Si-C	B_s = 1.2 T; H_c = 2–6 A/m; High resistivity	Up to 80 kW	Excellent loss performance	Noise issues; Brittleness
Ferrites	Mn-Zn Ferrite	B_s = 0.5–0.6 T; H_c = 2–6 A/m; High resistivity	<50 kW	High resistivity; Low eddy current loss	Low saturation flux density
Si-Steel (Electrical Steel)	Fe-3%Si	B_s = 1.8–2.0 T; H_c = 40–80 A/m;	>100 kW	High saturation flux density	High core losses at high frequencies
Powder Core	Fe-Si-Al (Sendust)	B_s = 1.0–1.2 T; H_c = 10–20 A/m; High resistivity	Up to 50 kW	Good high-frequency performance	Limited permeability

However, the large-scale manufacture of motors inevitably introduces factors that may affect the properties of materials. Processes such as cutting, punching, and heat treatment can induce mechanical and thermal stresses, leading to microstructural changes such as grain coarsening, defect formation, or partial amorphization. These changes may reduce the crystallinity of nanocrystalline alloys, affecting their soft magnetic properties, including increased losses and decreased permeability [124].

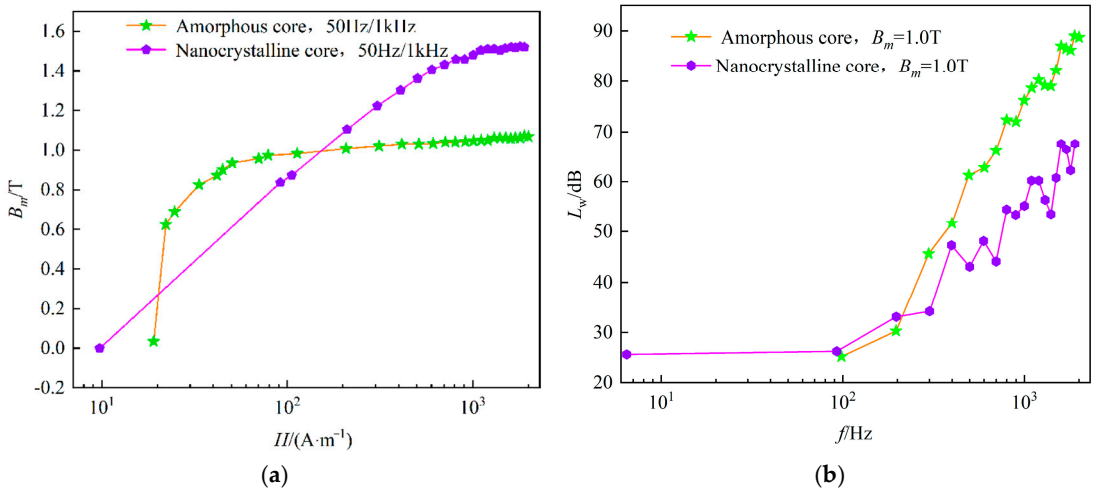
To address these challenges, advanced alloy designs incorporating grain boundary stabilizers, such as Cu, Nb, or Mo, have been developed to enhance thermal and structural stability. Post-processing techniques, such as stress-relief annealing and controlled heat treatments, can restore the crystallinity or mitigate the effects of structural disorder. Grain boundary complexion diagrams have been developed to predict interfacial structure and composition in binary and ternary alloys, which is particularly relevant for complex alloys [125].

5.1. Amorphous and Nanocrystalline Alloy Requirements

Mechanical stability is a special requirement for soft magnetic materials when it comes to their application in electrical machines, especially the stator cores. However, the major challenge lies not only in the accurate analysis and simulation of complex unfavorable external conditions but also the improvement of existing ribbon manufacturing techniques.

Soft magnetic materials, such as amorphous and nanocrystalline alloys, are mainly used as stator cores of motors. The power and efficiency performance of motors depends on various factors, such as their size, speed, thermal efficiency, and magnetic utilization. However, the average operating efficiency of the existing main series motor was only 87.6% [126]. As power density increases, high-performance magnetic materials are crucial for ensuring reliability and minimizing power loss. Therefore, the magnetic material targeted must have superior thermal, electromagnetic, and mechanical properties. The requirements of the material performance include high thermal conductivity, high electrical resistivity, high saturation magnetization, and low coercivity. Mechanical properties of the magnetic material require high yield strength, ductility, and fatigue strength.

Figure 10 demonstrates the differences in magnetic and mechanical properties of stator cores of motors [127]. When working at H of 100 A/m, the μ_r of amorphous and nanocrystalline cores remain constant. It is reported that amorphous stator core motors can achieve efficiency levels as high as 98%. However, the amorphous alloys present high acoustic noise sound pressure levels above 400 Hz, which is undoubtedly one of the major obstacles to its widespread use and areas of research focus. On the contrary, nanocrystalline alloys induce less noise.



(**a**) (**b**)

Figure 10. Comparison of magnetic and mechanical properties of stator cores in motors. (**a**) *B-H* curves of amorphous and nanocrystalline cores; (**b**) *L-f* curves of amorphous and nanocrystalline cores. Data from [127].

Amorphous and nanocrystalline alloys are intrinsically thin and hard, which increases the complexity of the coiling technique and limits the manufactured dimensions. Power loss would increase when the materials were fabricated into motor cores. In addition, the thermal conductivity of nanocrystalline materials is reduced due to the interfacial scattering of nanomaterials, which is a challenge for the thermal management of motor stator cores. The use of nanocrystalline materials for motor stator cores also faces the challenges of relatively high costs, limited magnetic and thermal conductivity, and low μ values. Overall, the soft magnetic composites, with their low cost, isotropic nature, and net-shaping, have made them competitive candidates for applications in stator cores of power motors [128].

5.2. Performance Analysis of Stator Cores

5.2.1. Vibration and Noise of Stator Cores

Understanding vibration mechanisms is the premise for accurately predicting and optimizing the operating properties. The radial vibrations of stator cores result from the interactive effects of magnetostriction stress and Maxwell stress (Maxwell stress is the key

point). The vibration behaviors of amorphous alloy, high silicon steel, and conventional steel were measured and compared in [129]. Figure 11 shows the Campbell diagram under squared flux density excitation. In addition, not only the 2nd harmonic trajectory but also the trajectory of the multiples of the 2nd harmonic are clearly shown in the figure. It turned out that the amorphous alloy exhibits a significantly higher sound pressure level than the other two materials, as shown in Figure 11. It can reach 101.6 dB of peak value under square flux voltage excitation.

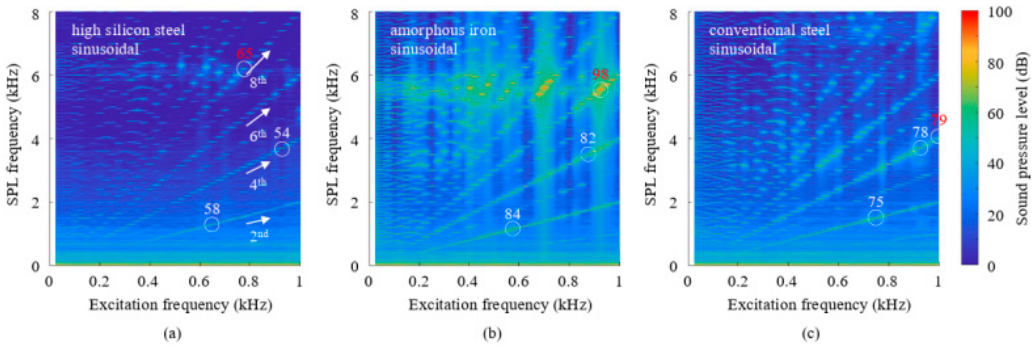


Figure 11. Comparison of sound pressure level (SPL) of (**a**) high silicon steel, (**b**) amorphous iron, and (**c**) conventional steel under square flux density excitation. Copyright [129].

However, it can be reduced by the regulation of flux density inside the stator cores. Meanwhile, the magnetostriction stress assumes a greater role in intensifying vibration as the rotating speed increases. The uneven distribution of Maxwell force and magnetostriction stress is attributed to the air gap eccentricity caused by slots and eccentricity. The eccentricity of stators and rotors is composed of static eccentricity, dynamic eccentricity, inclined eccentricity, and mixed eccentricity [130,131].

The aforementioned factors all result in direct relative displacement, leading to distortion of the magnetic flux field. Figure 12 shows the prominent spikes of slotted cores in contrast with the smooth curves of slotless ones. Additionally, there exists a negative correlation between the orders of harmonics and the level of vibration, which agrees with FEA results. Therefore, to obtain a more accurate simulation of open-circuit magnetic field distribution, it is essential to take slotted effects into consideration.

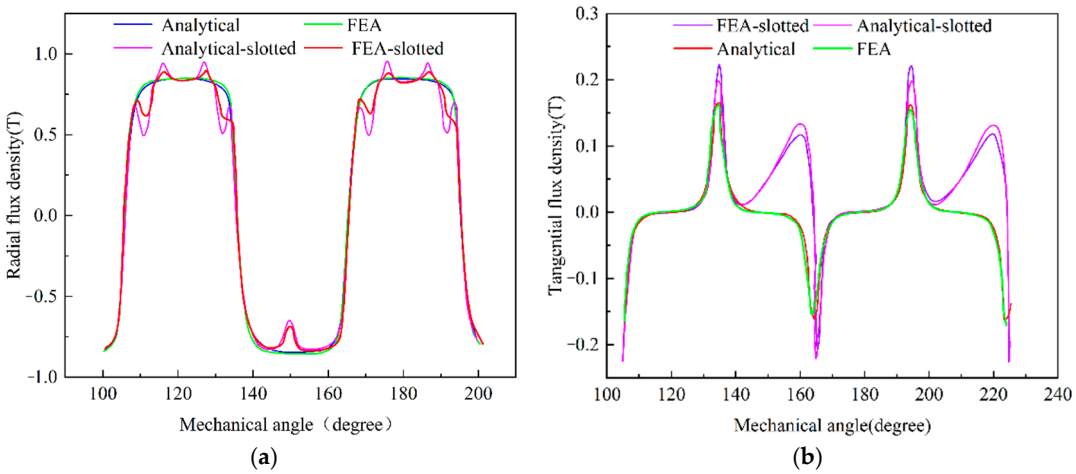


Figure 12. Flux density of permanent amorphous magnet motor with (**a**) radial components and (**b**) tangential components. Data from [132].

Based on the analysis above, three parameters can be chosen as indicators for motor operation, i.e., displacement, velocity, and acceleration. The root mean square value

of circumferential displacement demonstrates a non-linear increase as the rotary speed increases. The radial vibrations of stator cores are a result of the combined effects of magnetostriction stress and Maxwell stress, with Maxwell stress being the dominant factor [132].

5.2.2. Temperature Rise and Cooling

The temperature rise in amorphous motors is higher than that in silicon steel motors at rated rotating speed. This is mainly due to the low thermal conductivity of amorphous alloy than that of silicon steel. The power loss of amorphous motors at high frequencies, however, is lower compared to that of silicon steel motors, thereby offering advantageous prospects for the application of high-frequency amorphous motors [133]. Similar to transformers and inductors, the thermal behaviors of motors can be modeled by the TNM method. The heat coefficients of electrical motors in equivalent thermal networks are determined by single value decomposition (SVD) during the early stages [134].

Most of the drive motors for electric vehicles utilize water cooling to mitigate temperature rise [135]. However, researchers are exploring alternatives to water cooling devices due to their exorbitant cost and unwieldy dimensions, among which air cooling stands out as a viable option. Air cooling can be achieved by circulating air through gaps between windings at the drive end and the non-drive end of motors.

5.3. Design and Manufacturing of Power Motor

Designing motors with ribbon magnetic materials usually involves composition engineering and geometry optimization. Fe-Ni-based material can reduce the core loss to 3 W at rated power and 100 Hz [136]. A proposed stator core consists of an inner layer made of Metglas 2605SA1 and an outer layer made of Metglas 50A1000, and it reduces back electromotive force compared with conventional cores [137]. A synchronous electrical machine featuring unequal teeth width was built with amorphous alloys [138,139].

A modular stator with laminated teeth supplying radial flux embedded in the amorphous winding yoke was proposed, providing circumferential and axial flux [140]. Hybrid excitation motors, which combine permanent magnet motors and electric excitation motors, have gained popularity in this endeavor. It can enhance the magnetization by 39.9%. To produce amorphous strips, a laminated cutting method can be used, where the material undergoes a series of processes, starting with cutting and laminating, followed by molding, heat treating and solidifying, and, finally, shaping the stator core by wire cutting or milling. Figure 13 exhibits an example of an electrical machine made with an amorphous core and another with amorphous teeth, characterized by cutting or shearing ribbon.

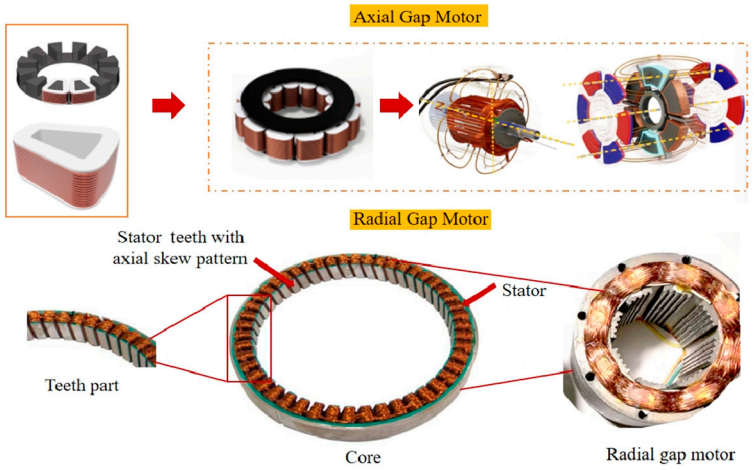


Figure 13. Examples of amorphous motors.

The utilization of nanocomposite amorphous alloy has facilitated the spatial engineering of μ of motors, thereby underscoring the imperative for laminate engineering. Some instances of manufacturing processes necessitating precise control include the manipulation of local crystallographic texture and in-line processing involving masking and strip alloys, as well as the induction of anisotropy through strain, field, and rolling. One study employed very important band treatment techniques, including heat treatment, thermal magnetic treatment, and thermo-mechanical treatments, such as stress annealing and magnetic field annealing. In addition, a triangular core bonded with epoxy resin is proposed in this study to securely hold the stator [141].

6. Concluding Remarks and Prospects

Amorphous and nanocrystalline alloys are excellent candidates for applications in lighter, smaller power electronic converters due to their excellent soft magnetic properties, such as high permeability, saturation magnetization, and Curie temperature and low coercivity and power loss. The heat treatment-induced embrittlement, the complicated composition, and the strict manufacturing process present the key issues in power device manufacture. Hence, research and development into the promotion of metal amorphous nanocomposites, especially nanocrystalline and soft magnetic composites, are necessary for the next power conversion.

The development of amorphous cores faces technical challenges due to the unique properties of these materials, such as their disordered atomic structure and the need for precise control over cooling rates during production. Achieving uniform properties across large areas is particularly difficult because even slight variations in cooling rates can lead to significant changes in magnetic performance and structural integrity. Meanwhile, the complex fabrication procedure, lengthy compositions, and, thereby, the expensive costs limit the application of nanocrystalline and soft magnetic composite cores. Life cycle analysis of the manufacturing process and the role of each element, thus, need to be carefully examined to resolve the issues of low thermal conductivity and mechanical brittleness.

Another important factor is the secure and stable real operation of cores fixed in power electronic converters. Except for material property optimization, local overheating, insulation, undesirable acoustic noise, and mechanical distortion should be integrated into the design of magnetic cores. Mechanical and thermal characteristics transformation from as-manufactured ribbons to the final geometry like toroidal cores should be carefully studied. FEM modeling and experiment verification are very essential to the design and application. Finally, artificial intelligence and machine learning can be integrated into the implementation of power electronic converters to improve efficiency and performance. The correlation between alloy composition and properties can be established, and possible new materials can be predicted by machine learning models, such as Support Vector Machines (SVMs). It can also predict the effects of different compositions and process parameters on the properties of nanocrystalline alloys.

The microscopic mechanisms of magnetic phenomena in metallic amorphous nanocrystalline alloys are suggested to be investigated afterward, where domain wall motion should be in the scope of the study. Domain wall motion is the movement of the boundary between regions of magnetic material with the direction of magnetization in response to an external magnetic field. Permeability engineering is precisely the design and manipulation of the magnetic properties of materials by controlling factors such as the wall motion of magnetic domains, microstructure, and composition. Consequently, low-crystal volume and composition optimization of nanocrystalline alloys are expected to be realized.

Future research will focus on the 3D magnetization behavior of metallic amorphous nanocomposites and soft magnetic composites, as well as on the concept of spatially

tunable permeability engineering, which opens up new possibilities for electromagnetism applications, in particular in terms of improving energy efficiency and power density. Spatially tunable permeability engineering refers to the advanced technique of deliberately varying the magnetic permeability across different regions of a magnetic material or device. It allows for the optimization of electromagnetic performance by tailoring the magnetic field distribution and reducing losses. In practical applications, a multi-physical field design optimization is presented, which involves the tuning of permeability curves in the inductor and converter design, followed by the simultaneous optimization of both the geometry and permeability of a given device considering the spatially correlated permeability engineering [142]. Spatially tunable permeability engineering has the potential to be extended to strain annealing technology and control.

With the widespread application of power electronics in electric vehicles, renewable energy systems, smart grids, and defense infrastructure, magnetic components have demonstrated significant potential in external noise suppression and electromagnetic interference (EMI) protection. The design of nanocrystalline and amorphous alloys enables effective absorption and shielding of high-frequency noise. Structural optimizations, such as distributed air gaps and multilayer winding configurations, further enhance noise suppression capabilities.

Research directions such as cloud services and digital twins can enable intelligent design and manufacturing of EM devices, considering the lifetime performance and reliability control [143]. Future research should focus on building large-scale, cross-material, structure, and application databases to support AI model training, as well as developing multi-physics-coupled modeling techniques. The combined effects of electromagnetic, thermal, and mechanical factors on material performance should be considered, thereby accelerating innovation in the field of power electronics.

Author Contributions: Conceptualization, W.W. and J.F.; methodology, C.L., W.W. and J.L.; formal analysis, J.F., Y.Y. and W.W.; investigation, J.F., C.L. and Y.Y.; resources, S.L. and A.W.; writing—original draft preparation, Y.Y. and A.W.; writing—review and editing, J.F., C.L. and W.W.; funding acquisition, W.W. All authors have read and agreed to the published version of the manuscript.

Funding: This research was funded by the National Natural Science Foundation of China (NSFC, No. 52177025).

Conflicts of Interest: The authors declare no conflicts of interest.

References

1. Granata, S.; Di Benedetto, M.; Terlizzi, C.; Leuzzi, R.; Bifaretti, S.; Zanchetta, P. Power Electronics Converters for the Internet of Energy: A Review. *Energies* **2022**, *15*, 2604. [CrossRef]
2. Silveyra, J.M.; Ferrara, E.; Huber, D.L.; Monson, T.C. Soft magnetic materials for a sustainable and electrified world. *Science* **2018**, *362*, eaao0195. [CrossRef] [PubMed]
3. Talaat, A.; Suraj, M.V.; Byerly, K.; Wang, A.; Wang, Y.; Lee, J.K.; Ohodnicki, P.R. Review on soft magnetic metal and inorganic oxide nanocomposites for power applications. *J. Alloys Compd.* **2021**, *870*, 159500. [CrossRef]
4. Balasubramanian, B.; Manchanda, P.; Pahari, R.; Chen, Z.; Zhang, W.Y.; Valloppilly, S.R.; Li, X.Z.; Sarella, A.; Yue, L.P.; Ullah, A.; et al. Chiral Magnetism and High-Temperature Skyrmions in B20-Ordered Co-Si. *Phys. Rev. Lett.* **2020**, *124*, 057201. [CrossRef]
5. Zhang, W.Y.; Balasubramanian, B.; Ullah, A.; Pahari, R.; Li, X.Z.; Yue, L.P.; Valloppilly, S.R.; Sokolov, A.; Skomski, R.; Sellmyer, D.J. Comparative study of topological Hall effect and skyrmions in NiMnIn and NiMnGa. *Appl. Phys. Lett.* **2019**, *115*, 172404. [CrossRef]
6. Mallakpour, S.; Khadem, E. Carbon nanotube-metal oxide nanocomposites: Fabrication, properties and applications. *Chem. Eng. J.* **2016**, *302*, 344–367. [CrossRef]

7. Zhang, Q.H.; Zhou, Z.X.; Dylla, M.; Agne, M.T.; Pei, Y.Z.; Wang, L.J.; Tang, Y.S.; Liao, J.C.; Li, J.; Bai, S.Q.; et al. Realizing high-performance thermoelectric power generation through grain boundary engineering of skutterudite-based nanocomposites. *Nano Energy* **2017**, *41*, 501–510. [CrossRef]
8. Inoue, A.; Zhang, T.; Takeuchi, A. Ferrous and Nonferrous Bulk Amorphous Alloys. *Mater. Sci. Forum* **1998**, *269–272*, 855–864. [CrossRef]
9. Yoshizawa, Y.; Oguma, S.; Yamauchi, K. New Fe-based soft magnetic-alloys composed of ultrafine grain-structure. *J. Appl. Phys.* **1988**, *64*, 6044–6046. [CrossRef]
10. Makino, A. Nanocrystalline Soft Magnetic Fe-Si-B-P-Cu Alloys with High *B* of 1.8–1.9T Contributable to Energy Saving. *IEEE Trans. Magn.* **2012**, *48*, 1331–1335. [CrossRef]
11. Suzuki, K.; Makino, A.; Inoue, A.; Masumoto, T. Soft magnetic properties of nanocrystalline bcc Fe-Zr-B and Fe-M-B-Cu (M=transition metal) alloys with high saturation magnetization (invited). *J. Appl. Phys.* **1991**, *70*, 6232–6237. [CrossRef]
12. Duwez, P.; Lin, S.C.H. Amorphous Ferromagnetic Phase in Iron-Carbon-Phosphorus Alloys. *J. Appl. Phys.* **1967**, *38*, 4096–4097. [CrossRef]
13. Shokrollahi, H.; Janghorban, K. Soft magnetic composite materials (SMCs). *J. Mater. Process. Technol.* **2007**, *189*, 1–12. [CrossRef]
14. Nogués, J.; Sort, J.; Langlais, V.; Skumryev, V.; Suriñach, S.; Muñoz, J.S.; Baró, M.D. Exchange bias in nanostructures. *Phys. Rep. Rev. Sec. Phys. Lett.* **2005**, *422*, 65–117. [CrossRef]
15. Yamaura, S.; Furuya, Y.; Watanabe, T. The effect of grain boundary microstructure on Barkhausen noise in ferromagnetic materials. *Acta Mater.* **2001**, *49*, 3019–3027. [CrossRef]
16. Herzer, G. Modern soft magnets: Amorphous and nanocrystalline materials. *Acta Mater.* **2013**, *61*, 718–734. [CrossRef]
17. Ullah, A.; Balasubramanian, B.; Tiwari, B.; Giri, B.; Sellmyer, D.J.; Skomski, R.; Xu, X.S. Topological spin textures and topological Hall effect in centrosymmetric magnetic nanoparticles. *Phys. Rev. B* **2023**, *108*, 184432. [CrossRef]
18. Herzer, G. Soft-magnetic nanocrystalline materials. *Scr. Metall. Mater.* **1995**, *33*, 1741–1756. [CrossRef]
19. Xiao, M.; Zheng, Z.G.; Ji, L.; Liu, X.; Qiu, Z.G.; Zeng, D.C. The role of V and Mo on crystallization process and magnetic properties of FeSiBCuNb alloys using in wide frequency scale. *J. Non Cryst. Solids* **2019**, *521*, 119546. [CrossRef]
20. Willard, M.A.; Daniil, M.; Kniping, K.E. Nanocrystalline soft magnetic materials at high temperatures: A perspective. *Scr. Mater.* **2012**, *67*, 554–559. [CrossRef]
21. Herzer, G. Magnetization process in nanocrystalline ferromagnets. *Mater. Sci. Eng. A Struct. Mater. Prop. Microstruct. Process.* **1991**, *133*, 1–5. [CrossRef]
22. Flohrer, S.; Schäfer, R.; McCord, J.; Roth, S.; Schultz, L.; Fiorillo, F.; Günther, W.; Herzer, G. Dynamic magnetization process of nanocrystalline tape wound cores with transverse field-induced anisotropy. *Acta Mater.* **2006**, *54*, 4693–4698. [CrossRef]
23. Kolano, R.; Kolano-Burian, A.; Polak, M.; Szynowski, J. Application of Rapidly Quenched Soft Magnetic Materials in Energy-Saving Electric Equipment. *IEEE Trans. Magn.* **2014**, *50*, 2004804. [CrossRef]
24. Silveyra, J.M.; Xu, P.; Keylin, V.; DeGeorge, V.; Leary, A.; McHenry, M.E. Amorphous and Nanocomposite Materials for Energy-Efficient Electric Motors. *J. Electron. Mater.* **2016**, *45*, 219–225. [CrossRef]
25. Pfützner, H.; Shilyashki, G.; Christodoulou, N. Standardisation concept for rapid testing of effects of cutting on losses of electric steel and amorphous ribbon. *IET Electr. Power Appl.* **2024**, *18*, 1164–1173. [CrossRef]
26. Theisen, E.A. Recent Advances and Remaining Challenges in Manufacturing of Amorphous and Nanocrystalline Alloys. *IEEE Trans. Magn.* **2022**, *58*, 2001207. [CrossRef]
27. Jin, J.X.; Tang, Y.J.; Xiao, X.Y.; Du, B.X.; Wang, Q.L.; Wang, J.H.; Wang, S.H.; Bi, Y.F.; Zhu, J.G. HTS Power Devices and Systems: Principles, Characteristics, Performance, and Efficiency. *IEEE Trans. Appl. Supercond.* **2016**, *26*, 3800526. [CrossRef]
28. Shadfar, H.; Pashakolaei, M.G.; Foroud, A.A. Solid-state transformers: An overview of the concept, topology, and its applications in the smart grid. *Int. Trans. Electr. Energy Syst.* **2021**, *31*, e12996. [CrossRef]
29. Islam, M.R.; Lei, G.; Guo, Y.G.; Zhu, J.G. Optimal Design of High-Frequency Magnetic Links for Power Converters Used in Grid-Connected Renewable Energy Systems. *IEEE Trans. Magn.* **2014**, *50*, 2006204. [CrossRef]
30. Islam, M.R.; Mahfuz-Ur-Rahman, A.M.; Islam, M.M.; Guo, Y.G.G.; Zhu, J.G.G. Modular Medium-Voltage Grid-Connected Converter with Improved Switching Techniques for Solar Photovoltaic Systems. *IEEE Trans. Ind. Electron.* **2017**, *64*, 8887–8896. [CrossRef]
31. Li, Z.; Han, W.; Xin, Z.; Liu, Q.; Chen, J.; Loh, P.C. A Review of Magnetic Core Materials, Core Loss Modeling and Measurements in High-Power High-Frequency Transformers. *CPSS Trans. Power Electron. Appl.* **2022**, *7*, 359–373. [CrossRef]
32. Liu, J.; Mei, Y.; Lu, G. Development of High-frequency Soft Magnetic Materials for Power Electronics. *J. Mater. Eng.* **2017**, *45*, 127–134.
33. Bashir-U-Din, A. Characterisation of Amorphous Metal Materials for High-Frequency High-Power-Density Transformer. In Proceedings of the 26th International Conference on Systems Engineering (ICSEng), University of Technology Sydney, Sydney, Australia, 18–20 December 2018.

34. Leary, A.M.; Ohodnicki, P.R.; McHenry, M.E. Soft Magnetic Materials in High-Frequency, High-Power Conversion Applications. *JOM* **2012**, *64*, 772–781. [CrossRef]
35. Islam, M.R.; Muttaqi, K.M.; Sutanto, D.; Zhu, J.G. Design and Implementation of Amorphous Magnetic Material Common Magnetic Bus for the Replacement of Common DC Bus. *IEEE Trans. Magn.* **2018**, *54*, 2002004. [CrossRef]
36. VK GmbH & Co. Properties of Amorphous Co-Based Alloys with F-Characteristics. Available online: https://www.vacuumschmelze.com/products (accessed on 30 November 2024).
37. Ohta, M.; Hasegawa, R. Soft Magnetic Properties of Magnetic Cores Assembled with a High B_s Fe-Based Nanocrystalline Alloy. *IEEE Trans. Magn.* **2017**, *53*, 2000205. [CrossRef]
38. Ohta, M.; Hasegawa, R.; Itabashi, H. Development of Block Cores Comprising High-B_s Nanocrystalline Alloy Ribbon. *IEEE Trans. Magn.* **2018**, *54*, 2000504. [CrossRef]
39. Yoshizawa, Y.; Ohta, M. Magnetic properties of nanocrystalline Fe-Cu-Si-B alloys. In Proceedings of the 13th International Conference on Rapidly Quenched and Metastable Materials, Dresden, Germany, 24–29 August 2008.
40. Makino, A.; Men, H.; Kubota, T.; Yubuta, K.; Inoue, A. FeSiBPCu Nanocrystalline Soft Magnetic Alloys with High B_s of 1.9 Tesla Produced by Crystallizing Hetero-Amorphous Phase. *Mater. Trans.* **2009**, *50*, 204–209. [CrossRef]
41. Ruiz-Robles, D.; Figueroa-Barrera, C.; Moreno-Goytia, E.L.; Venegas-Rebollar, V. An Experimental Comparison of the Effects of Nanocrystalline Core Geometry on the Performance and Dispersion Inductance of the MFTs Applied in DC-DC Converters. *Electronics* **2020**, *9*, 453. [CrossRef]
42. Azuma, D.; Ito, N.; Ohta, M. Recent progress in Fe-based amorphous and nanocrystalline soft magnetic materials. *J. Magn. Magn. Mater.* **2020**, *501*, 166373. [CrossRef]
43. Francoeur, B.; Couture, P. Continuous-annealing method for producing a flexible, curved, soft magnetic amorphous alloy ribbon. *J. Appl. Phys.* **2012**, *111*, 07A309. [CrossRef]
44. Lin, K.C.; Zook, E.E.; Crockett, J.W. Material usage in stacked transformer cores. *J. Mater. Eng.* **1990**, *12*, 51–57. [CrossRef]
45. Fukunaga, H.; Eguchi, T.; Koga, K.; Ohta, Y.; Kakehashi, H. High-performance cut cores prepared from crystallized Fe-based amorphous ribbon. *IEEE Trans. Magn.* **1990**, *26*, 2008–2010. [CrossRef]
46. Imaoka, J.; Okamoto, K.; Shoyama, M.; Ishikura, Y.; Noah, M.; Yamamoto, M. Modeling, Magnetic Design, Simulation Methods, and Experimental Evaluation of Various Powder Cores Used in Power Converters Considering Their DC Superimposition Characteristics. *IEEE Trans. Power Electron.* **2019**, *34*, 9033–9051. [CrossRef]
47. Lakatos-Varsányi, M.; Mikó, A.; Varga, L.K.; Kálmán, E. Electrodeposited magnetic multi-nano-layers. *Corros. Sci.* **2005**, *47*, 681–693. [CrossRef]
48. Varga, L.K. Soft magnetic nanocomposites for high-frequency and high-temperature applications. *J. Magn. Magn. Mater.* **2007**, *316*, 442–447. [CrossRef]
49. Fujimori, H.; Ohnuma, S.; Kobayashi, N.; Masumoto, T. Spintronics in metal-insulator nanogranular magnetic thin films. *J. Magn. Magn. Mater.* **2006**, *304*, 32–35. [CrossRef]
50. Ohnuma, S.; Ohnuma, M.; Fujimori, H.; Masumoto, T. Metal-insulator type nano-granular soft magnetic thin films investigations on mechanism and applications. *J. Magn. Magn. Mater.* **2007**, *310*, 2503–2509. [CrossRef]
51. Naoe, M.; Sonehara, M.; Miyaji, K.; Sato, T.; Endo, Y.; Kobayashi, N.; Arai, K.I. Crossed anisotropy multilayered nanogranular films combining high permeability, ferromagnetic resonance frequency, and resistivity. In Proceedings of the 2023 IEEE International Magnetic Conference-Short Papers (INTERMAG Short Papers), Sendai, Japan, 15–19 May 2023; pp. 1–2. [CrossRef]
52. Luo, Z.C.; Li, X.R.; Jiang, C.Q.; Long, T. Characterization of Nanocrystalline Flake Ribbon for High Frequency Magnetic Cores. *IEEE Trans. Power Electron.* **2022**, *37*, 14011–14016. [CrossRef]
53. Bertotti, G. General-properties of power losses in soft ferromagnetic materials. *IEEE Trans. Magn.* **1988**, *24*, 621–630. [CrossRef]
54. Liu, F.-g.; Zhao, L.; Jiang, J.-c. Calculation and verification of core loss of high frequency transformer under sinusoidal and non-sinusoidal excitation. *Adv. Technol. Electr. Eng. Energy* **2021**, *40*, 25–32. [CrossRef]
55. Li, C.; Xu, Q. Modeling of Temperature Dependent Hysteresis Based on Preisach Theory. *Trans. China Electrotech. Soc.* **2013**, *28*, 90–94.
56. Shi, Y.M.; Jiles, D.C.; Ramesh, A. Generalization of hysteresis modeling to anisotropic and textured materials. *J. Magn. Magn. Mater.* **1998**, *187*, 75–78. [CrossRef]
57. Sablik, M.J.; Jiles, D.C. Coupled magnetoelastic theory of magnetic and magnetostrictive hysteresis. *IEEE Trans. Magn.* **1993**, *29*, 2113–2123. [CrossRef]
58. Raghunathan, A.; Melikhov, Y.; Snyder, J.E.; Jiles, D.C. Modeling the Temperature Dependence of Hysteresis Based on Jiles-Atherton Theory. *IEEE Trans. Magn.* **2009**, *45*, 3954–3957. [CrossRef]
59. Gao, Y.H.; Araki, Y.; Dozono, H.; Muramatsu, K.; Guan, W.M.; Yuan, J.X.; Tian, C.H.; Chen, B.C. Modeling of Anomalous Eddy Current Losses Due to Movement of Domain Walls in Particles of a Soft Magnetic Composite. *IEEE Trans. Magn.* **2020**, *56*, 7515904. [CrossRef]

60. Pry, R.H.; Bean, C.P. Calculation of The Energy Loss in Magnetic Sheet Materials Using a Domain Model. *J. Appl. Phys.* **1958**, *29*, 532–533. [CrossRef]
61. Mayergoyz, I.D. Mathematical-models of hysteresis. *IEEE Trans. Magn.* **1986**, *22*, 603–608. [CrossRef]
62. Adly, A.A.; Mayergoyz, I.D.; Bergqvist, A. Preisach modeling of magnetostrictive hysteresis. *J. Appl. Phys.* **1991**, *69*, 5777–5779. [CrossRef]
63. Stoner, E.C.; Wohlfarth, E.P. A mechanism of magnetic hysteresis in heterogeneous alloys. *Philos. Trans. R. Soc. Lond. Ser. A Math. Phys. Sci.* **1948**, *240*, 599–642. [CrossRef]
64. Jiles, D.C.; Atherton, D.L. Theory of ferromagnetic hysteresis. *J. Appl. Phys.* **1984**, *55*, 2115–2120. [CrossRef]
65. Venkatachalam, K.; Sullivan, C.R.; Abdallah, T.; Tacca, H. Accurate prediction of ferrite core loss with nonsinusoidal waveforms using only Steinmetz parameters. In Proceedings of the 8th Workshop on Computers in Power Electronics, University of Puerto Rico, Mayaguez, Puerto Rico, 3–4 June 2002; pp. 36–41.
66. Van den Bossche, A.; Valchev, V.C.; Georgiev, G.B. Measurement and loss model of ferrites with non-sinusoidal waveforms. In Proceedings of the 35th Annual IEEE Power Electronics Specialists Conference (PESC 04), Aachen, Germany, 20–25 June 2004; pp. 4814–4818.
67. Shen, W.; Wang, F.; Boroyevich, D.; Tipton, C.W. Loss characterization and calculation of nanocrystalline cores for high-frequency magnetics applications. In Proceedings of the 22nd Annual IEEE Applied Power Electronics Conference (APEC 2007), Anaheim, CA, USA, 25 February–1 March 2007; pp. 475–484.
68. Reinert, J.; Brockmeyer, A.; De Doncker, R.W. Calculation of losses in ferro- and ferrimagnetic materials based on the modified Steinmetz equation. In Proceedings of the Conference Record of the 1999 IEEE Industry Applications Conference. Thirty-Forth IAS Annual Meeting (Cat. No.99CH36370), Phoenix, AZ, USA, 3–7 October 1999; Volume 2083, pp. 2087–2092. [CrossRef]
69. Li, J.L.; Abdallah, T.; Sullivan, C.R. Improved calculation of core loss with nonsinusoidal waveforms. In Proceedings of the 36th Annual Meeting of the Industry-Application-Society (IAS), Chicago, IL, USA, 30 September–4 October 2000; pp. 2203–2210.
70. He, S.; Yongjian, L.; Xinran, Y.; Shuaichao, Y.; Ming, Y. Research of Harmonic Effects on Core Loss in Soft Magnetic Composite Materials Based on Three-Dimensional Magnetic Test System. In Proceedings of the 2019 22nd International Conference on Electrical Machines and Systems (ICEMS), Harbin, China, 11–14 August 2019; pp. 1–5. [CrossRef]
71. Villar, I.; Viscarret, U.; Etxeberria-Otadui, I.; Rufer, A. Global Loss Evaluation Methods for Nonsinusoidally Fed Medium-Frequency Power Transformers. *IEEE Trans. Ind. Electron.* **2009**, *56*, 4132–4140. [CrossRef]
72. Mühlethaler, J.; Biela, J.; Kolar, J.W.; Ecklebe, A. Improved Core-Loss Calculation for Magnetic Components Employed in Power Electronic Systems. *IEEE Trans. Power Electron.* **2012**, *27*, 964–973. [CrossRef]
73. Barg, S.; Ammous, K.; Mejbri, H.; Ammous, A. An Improved Empirical Formulation for Magnetic Core Losses Estimation Under Nonsinusoidal Induction. *IEEE Trans. Power Electron.* **2017**, *32*, 2146–2154. [CrossRef]
74. Zhao, H.Y.; Ragusa, C.; Appino, C.; de la Barrière, O.; Wang, Y.H.; Fiorillo, F. Energy Losses in Soft Magnetic Materials Under Symmetric and Asymmetric Induction Waveforms. *IEEE Trans. Power Electron.* **2019**, *34*, 2655–2665. [CrossRef]
75. Ahn, H.M.; Oh, Y.H.; Kim, J.K.; Song, J.S.; Hahn, S.C. Experimental Verification and Finite Element Analysis of Short-Circuit Electromagnetic Force for Dry-Type Transformer. *IEEE Trans. Magn.* **2012**, *48*, 819–822. [CrossRef]
76. Wu, W.; Kern, J.A. Temperature rise prediction of a natural cooling dry-type transformer. In Proceedings of the SoutheastCon 2016, Norfolk, VA, USA, 30 March–3 April 2016.
77. Lee, M.; Abdullah, H.A.; Jofriet, J.C.; Patel, D. Temperature distribution in foil winding for ventilated dry-type power transformers. *Electr. Power Syst. Res.* **2010**, *80*, 1065–1073. [CrossRef]
78. Smolka, J.; Nowak, A.J. Shape Optimization of Coils and Cooling Ducts in Dry-Type Transformers Using Computational Fluid Dynamics and Genetic Algorithm. *IEEE Trans. Magn.* **2011**, *47*, 1726–1731. [CrossRef]
79. Liu, C.; Ruan, J.J.; Wen, W.; Gong, R.H.; Liao, C.B. Temperature rise of a dry-type transformer with quasi-3D coupled-field method. *IET Electr. Power Appl.* **2016**, *10*, 598–603. [CrossRef]
80. Finocchio, M.A.F.; Lopes, J.J.; de França, J.A.; Piai, J.C.; Mangili, J.F. Neural networks applied to the design of dry-type transformers: An example to analyze the winding temperature and elevate the thermal quality. *Int. Trans. Electr. Energy Syst.* **2017**, *27*, e2257. [CrossRef]
81. Chen, Y.F.; Yang, Q.X.; Zhang, C.G.; Li, Y.J.; Li, X.H. Thermal Network Model of High-Power Dry-Type Transformer Coupled with Electromagnetic Loss. *IEEE Trans. Magn.* **2022**, *58*, 8402105. [CrossRef]
82. Yan, X.X.; Li, Y.J.; Cheng, Z.G.; Zhang, C.G. Prediction of temperature rise for ventilated dry-type transformer by 3-D coupled magneto-fluid-thermal model. *Int. J. Appl. Electromagn. Mech.* **2020**, *62*, 725–735. [CrossRef]
83. Sun, Y.Y.; Xu, G.D.; Li, N.; Li, K.J.; Liang, Y.L.; Zhong, H.; Zhang, L.N.; Liu, P. Hotspot Temperature Prediction of Dry-Type Transformers Based on Particle Filter Optimization with Support Vector Regression. *Symmetry* **2021**, *13*, 1320. [CrossRef]
84. Zhao, S.S.; Li, Q.; Lee, F.C. High Frequency Transformer Design for Modular Power Conversion from Medium Voltage AC to 400V DC. In Proceedings of the 32nd Annual IEEE Applied Power Electronics Specialists Conference and Exposition (APEC), Tampa, FL, USA, 26–30 March 2017; pp. 2894–2901.

85. Shuai, P.; Biela, J. Influence of Material Properties and Geometric Shape of Magnetic Cores on Acoustic Noise Emission of Medium-Frequency Transformers. *IEEE Trans. Power Electron.* **2017**, *32*, 7916–7931. [CrossRef]
86. Zhang, F.; Ji, S.C.; Shi, Y.H.; Zhu, L.Y. Investigation on the Action of Eddy Current on Tank Vibration Characteristics in Dry-Type Transformer. *IEEE Trans. Magn.* **2019**, *55*, 8400908. [CrossRef]
87. Moses, A.J.; Anderson, P.I.; Phophongviwat, T.; Tabrizi, S. Contribution of magnetostriction to transformer noise. In Proceedings of the 2010 45th International Universities Power Engineering Conference (UPEC 2010), Cardiff, UK, 31 August–3 September 2010; pp. 1–5.
88. Belahcen, A. *Magnetoelasticity, Magnetic Forces and Magnetostriction in Electrical Machines*; Helsinki University of Technology: Helsinki, Finland, 2004.
89. Weiser, B.; Pfützner, H.; Anger, J. Relevance of magnetostriction and forces for the generation of audible noise of transformer cores. *IEEE Trans. Magn.* **2000**, *36*, 3759–3777. [CrossRef]
90. Li, J.; Water, W.; Zhu, B.Y.; Lu, J.W. Integrated High-Frequency Coaxial Transformer Design Platform Using Artificial Neural Network Optimization and FEM Simulation. *IEEE Trans. Magn.* **2015**, *51*, 8500204. [CrossRef]
91. Ruiz-Robles, D.; Venegas-Rebollar, V.; Anaya-Ruiz, A.; Moreno-Goytia, E.L.; Rodríguez-Rodríguez, J.R. Design and Prototyping Medium-Frequency Transformers Featuring a Nanocrystalline Core for DC-DC Converters. *Energies* **2018**, *11*, 2081. [CrossRef]
92. Guo, Z.C.; Rajendran, S.; Tangudu, J.; Khakpour, Y.; Taylor, S.; Xing, L.; Xu, Y.; Feng, X.Y.; Huang, A.Q. A Novel High Insulation 100 kW Medium Frequency Transformer. *IEEE Trans. Power Electron.* **2023**, *38*, 112–117. [CrossRef]
93. Battal, F.; Balci, S.; Sefa, I. An Analysis of High Power Inductor Vibration Behavior in Terms of Air Gaps. In Proceedings of the 2019 International Conference on Power Generation Systems and Renewable Energy Technologies (PGSRET), Istanbul, Turkey, 26–27 August 2019; pp. 1–6. [CrossRef]
94. Jiang, C.Q.; Li, X.R.; Ghosh, S.S.; Zhao, H.; Shen, Y.F.; Long, T. Nanocrystalline Powder Cores for High-Power High-Frequency Power Electronics Applications. *IEEE Trans. Power Electron.* **2020**, *35*, 10821–10830. [CrossRef]
95. Yeo, J.G.; Kim, D.H.; Choi, Y.J.; Lee, B.W. Improving Power-Inductor Performance by Mixing Sub-micro Fe Powder with Amorphous Soft Magnetic Composites. *J. Electron. Mater.* **2019**, *48*, 6018–6023. [CrossRef]
96. Lara-Reyes, J.; Ponce-Silva, M.; Cortés-García, C.; Lozoya-Ponce, R.E.; Parrilla-Rubio, S.M.; García-García, A.R. High-Power-Factor LC Series Resonant Converter Operating Off-Resonance with Inductors Elaborated with a Composed Material of Resin/Iron Powder. *Electronics* **2022**, *11*, 3761. [CrossRef]
97. Soinski, M.; Leszczynski, J.; Swieboda, C.; Kwiecien, M. Nanocrystalline Block Cores for High-Frequency Chokes. *IEEE Trans. Magn.* **2014**, *50*, 2801904. [CrossRef]
98. Yan, Y.K.; Geng, L.W.D.; Zhang, L.J.; Tu, C.; Sriramdas, R.; Liu, H.R.; Li, X.T.; Sanghadasa, M.; Ngo, K.D.T.; Wang, Y.U.; et al. High-Power Magnetoelectric Voltage Tunable Inductors. *IEEE Trans. Ind. Electron.* **2021**, *68*, 5355–5365. [CrossRef]
99. Soinski, M.; Leszczynski, J.; Swieboda, C.; Kwiecien, M. The applicability of nanocrystalline stacked cores for power electronics. *Int. J. Appl. Electromagn. Mech.* **2015**, *48*, 301–307. [CrossRef]
100. Yang, R.S.; Hanson, A.J.; Perreault, D.J.; Sullivan, C.R. A Low-Loss Inductor Structure and Design Guidelines for High-Frequency Applications. In Proceedings of the 33rd Annual IEEE Applied Power Electronics Conference and Exposition (APEC), San Antonio, TX, USA, 4–8 March 2018; pp. 579–586.
101. Varga, L.K. High-Frequency Inductor Materials. *J. Electron. Mater.* **2014**, *43*, 117–120. [CrossRef]
102. Mao, X.; Chen, W. Winding loss mechanism analysis and the design for a new structure high-frequency gapped inductor. In Proceedings of the INTERMAG Asia 2005: Digest of the IEEE International Magnetics Conference (IEEE Cat. No.05CH37655), Nagoya, Japan, 4–8 April 2005; pp. 1073–1074. [CrossRef]
103. Neumayr, D.; Bortis, D.; Kolar, J.W.; Hoffmann, S.; Hoene, E. Origin and quantification of increased core loss in MnZn ferrite plates of a multi-gap inductor. *CPSS Trans. Power Electron. Appl.* **2019**, *4*, 72–93. [CrossRef]
104. Zhao, H.B.; Huang, Z.Z.; Dalal, D.N.; Jorgensen, J.K.; Jorgensen, A.B.; Wang, X.F.; Munk-Nielsen, S. Parasitic Capacitance Modeling of Copper-Foiled Medium-Voltage Filter Inductors Considering Fringe Electrical Field. *IEEE Trans. Power Electron.* **2021**, *36*, 8181–8192. [CrossRef]
105. Lai, Y.W.; Wang, S.; Zhang, B.Y. Investigation of Magnetic Field Immunity and Near Magnetic Field Reduction for the Inductors in High Power Density Design. *IEEE Trans. Power Electron.* **2019**, *34*, 5340–5351. [CrossRef]
106. Rossi, M.; Le Besnerais, J. Vibration Reduction of Inductors Under Magnetostrictive and Maxwell Forces Excitation. *IEEE Trans. Magn.* **2015**, *51*, 8403406. [CrossRef]
107. Du, B.X.; Liu, D.S. Dynamic Behavior of Magnetostriction-Induced Vibration and Noise of Amorphous Alloy Cores. *IEEE Trans. Magn.* **2015**, *51*, 7208708. [CrossRef]
108. Yoo, K.Y.; Lee, B.K.; Kim, D.H. Investigation of Vibration and Acoustic Noise Emission of Powder Core Inductors. *IEEE Trans. Power Electron.* **2019**, *34*, 3633–3645. [CrossRef]
109. Cuellar, C.; Benabou, A.; Idir, N. Characterization and Modeling of Hysteresis for Magnetic Materials Used in EMI Filters of Power Converters. *IEEE Trans. Power Electron.* **2014**, *29*, 4911–4920. [CrossRef]

110. Kovacic, M.; Hanic, Z.; Stipetic, S.; Krishnamurthy, S.; Zarko, D. Analytical Wideband Model of a Common-Mode Choke. *IEEE Trans. Power Electron.* **2012**, *27*, 3173–3185. [CrossRef]
111. Caponet, M.C.; Profumo, F.; Tenconi, A. EMI filters design for power electronics. In Proceedings of the 33rd IEEE Annual Power Electronics Specialists Conference (PESC02), Cairns, Australia, 23–27 June 2002; pp. 2027–2032.
112. Liu, Y.Z.; Ou, J.; Schiefer, M.; Breining, P.; Grilli, F.; Doppelbauer, M. Application of an Amorphous Core to an Ultra-High-Speed Sleeve-Free Interior Permanent-Magnet Rotor. *IEEE Trans. Ind. Electron.* **2018**, *65*, 8498–8509. [CrossRef]
113. Ismagilov, F.R.; Papini, L.; Vavilov, V.E.; Gusakov, D.V. Design and Performance of a High-Speed Permanent Magnet Generator with Amorphous Alloy Magnetic Core for Aerospace Applications. *IEEE Trans. Ind. Electron.* **2020**, *67*, 1750–1758. [CrossRef]
114. Celie, J.; Stie, M.; Rens, J.; Sergeant, P. Effects of cutting and annealing of amorphous materials for high speed permanent magnet machines. In Proceedings of the 22nd International Conference on Electrical Machines (ICEM), Lausanne, Switzerland, 4–7 September 2016; pp. 1630–1635.
115. Enomoto, Y.; Ito, M.; Koharagi, H.; Masaki, R.; Ohiwa, S.; Ishihara, C.; Mita, A. Evaluation of experimental permanent-magnet brushless motor utilizing new magnetic material for stator core teeth. *IEEE Trans. Magn.* **2005**, *41*, 4304–4308. [CrossRef]
116. Mischler, W.R.; Rosenberry, G.M.; Frischmann, P.G.; Tompkins, R.E. Test-Results on a Low-Loss Amorphous Iron Induction-Motor. *IEEE Trans. Power Appar. Syst.* **1981**, *100*, 2907–2911. [CrossRef]
117. Johnson, L.A.; Cornell, E.P.; Bailey, D.J.; Hegyi, S.M. Application of Low-Loss Amorphous Metals in Motors and Transformers. *IEEE Trans. Power Appar. Syst.* **1982**, *101*, 2109–2114. [CrossRef]
118. Jensen, C.C.; Profumo, F.; Lipo, T.A. A low loss permanent magnet brushless DC motor utilizing tape wound amorphous iron. In Proceedings of the Conference Record of the 1990 IEEE Industry Applications Society Annual Meeting (Cat. No.90CH2935-5), Seattle, WA, USA, 7–12 October 1990; Volume 281, pp. 281–286. [CrossRef]
119. Liew, G.S.; Ertugrul, N.; Wen Liang, S.; Gayler, J. Investigation of axial field permanent magnet motor utilising amorphous magnetic material. *Aust. J. Electr. Electron. Eng.* **2007**, *3*, 111–120. [CrossRef]
120. Wang, Z.; Masaki, R.; Morinaga, S.; Enomoto, Y.; Itabashi, H.; Ito, M.; Tanigawa, S. Development of an Axial Gap Motor with Amorphous Metal Cores. *IEEE Trans. Ind. Appl.* **2011**, *47*, 1293–1299. [CrossRef]
121. Fan, Z.Y.; Yi, H.; Xu, J.; Xie, K.; Qi, Y.; Ren, S.L.; Wang, H.D. Performance Study and Optimization Design of High-Speed Amorphous Alloy Induction Motor. *Energies* **2021**, *14*, 2468. [CrossRef]
122. Makino, A.; Hatanai, T.; Inoue, A.; Masumoto, T. Nanocrystalline soft magnetic Fe-M-B (M=Zr, Hf, Nb) alloys and their applications. *Mater. Sci. Eng. A Struct. Mater. Prop. Microstruct. Process.* **1997**, *226*, 594–602. [CrossRef]
123. Moses, A.J. Energy efficient electrical steels: Magnetic performance prediction and optimization. *Scr. Mater.* **2012**, *67*, 560–565. [CrossRef]
124. Rom, C.L.; Smaha, R.W.; O'Donnell, S.; Dugu, S.; Bauers, S.R. Emerging magnetic materials for electric vehicle drive motors. *MRS Bull.* **2024**, *49*, 738–750. [CrossRef]
125. Grigorian, C.M.; Rupert, T.J. Multi-principal element grain boundaries: Stabilizing nanocrystalline grains with thick amorphous complexions. *J. Mater. Res.* **2022**, *37*, 554–566. [CrossRef]
126. Chen, G.; Tu, G.; Lv, W. Applications of amorphous/nanocrystalline soft magnetic materials in high efficient motors. *J. Magn. Mater. Devics* **2012**, *43*, 1.
127. Li, S.H.; Li, L.J.; Jia, C.B.; Li, D.R.; Lu, Z.C. Study on Amorphous and Nanocrystalline Stator Cores for High-Speed Motor. *Small Spec. Electr. Mach.* **2019**, *47*, 9–12.
128. Jack, A.G.; Mecrow, B.C.; Dickinson, P.G.; Stephenson, D.; Burdess, J.S.; Fawcett, N.; Evans, J.T. Permanent-magnet machines with powdered iron cores and prepressed windings. *IEEE Trans. Ind. Appl.* **2000**, *36*, 1077–1084. [CrossRef]
129. Cai, Y.; El-faouri, F.S.; Saikawa, N.; Chiba, A. Measurement of Vibration and Acoustic Noise Generated by Magnetostriction in Three Stator Cores Made of High Silicon Steel, Amorphous Iron, and Conventional Silicon Steel. In Proceedings of the 2022 IEEE Energy Conversion Congress and Exposition (ECCE), Detroit, MI, USA, 9–13 October 2022; pp. 1–7. [CrossRef]
130. Sousa, K.M.; Dreyer, U.J.; Martelli, C.; da Silva, J.C.C. Dynamic Eccentricity Induced in Induction Motor Detected by Optical Fiber Bragg Grating Strain Sensors. *IEEE Sens. J.* **2016**, *16*, 4786–4792. [CrossRef]
131. McCloskey, A.; Arrasate, X.; Hernández, X.; Gómez, I.; Almandoz, G. Analytical calculation of vibrations of electromagnetic origin in electrical machines. *Mech. Syst. Signal Proc.* **2018**, *98*, 557–569. [CrossRef]
132. Xu, X.P.; Han, Q.K.; Qin, Z.Y.; Chu, F.L. Analytical methods for the radial electromagnetic vibration of stator in permanent magnet motors with an amorphous alloy core. *Mech. Syst. Signal Proc.* **2020**, *145*, 106909. [CrossRef]
133. Liu, R.; Zhu, J.; Cao, J. Temperature field analysis of silicon steel and amorphous on permanent magnet synchronous motors used in electrical vehicles. *J. Beijing Jiaotong Univ.* **2019**, *43*, 119–125.
134. Bousbaine, A.; McCormick, M.; Low, W.F. In-situ determination of thermal coefficients for electrical machines. *IEEE Trans. Energy Convers.* **1995**, *10*, 385–391. [CrossRef]
135. Sun, M.; Tang, R.; Han, X.; Tong, W. Temperature field analysis of a high frequency amorphous alloy axial flux permanent magnet machine with different cooling schemes. *Electr. Mach. Control* **2018**, *22*, 54–61.

136. Simizu, S.; Ohodnicki, P.R.; McHenry, M.E. Metal Amorphous Nanocomposite Soft Magnetic Material-Enabled High Power Density, Rare Earth Free Rotational Machines. *IEEE Trans. Magn.* **2018**, *54*, 8202505. [CrossRef]
137. Zaid, M.M.; Ahmad, H.; Sami, I.; Waheed, A.; Hussain Bukhari, S.S.; Ro, J.S. Design of a High Torque Density Interior Permanent Magnet Synchronous Machine with improved Efficiency using Amorphous Magnetic Material. In Proceedings of the 2021 IEEE International Magnetic Conference (INTERMAG), Lyon, France, 26–30 April 2021; pp. 1–4. [CrossRef]
138. Zhou, J.; Xiao, X. An Advanced High-Speed Permanent Magnet Synchronous Machine Utilizing Amorphous Alloy Core with Unequal Tooth Width. In Proceedings of the 2021 IEEE Sustainable Power and Energy Conference (iSPEC), Nanjing, China, 23–25 December 2021; pp. 3423–3427. [CrossRef]
139. Ismagilov, F.R.; Vavilov, V.E.; Gusakov, D.V.; Jing, O. High-speed generator with tooth-coil winding, permanent magnets and new design of a stator magnetic core made from amorphous alloy. In Proceedings of the 2018 25th International Workshop on Electric Drives: Optimization in Control of Electric Drives (IWED), Moscow, Russia, 31 January–2 February 2018; pp. 1–5. [CrossRef]
140. Wu, S.N.; Wang, Y.K.; Tong, W.M. Design and Analysis of New Modular Stator Hybrid Excitation Synchronous Motor. *CES Trans. Electr. Mach. Syst.* **2022**, *6*, 188–194. [CrossRef]
141. Ismagilov, F.R.; Wenming, T.; Vavilov, V.Y.; Gusakov, D.V.; Ayguzina, V.V. High-speed Electrical Machine with Radial Magnetic Flux and Stator Core Made of Amorphous Magnetic Material. Technologies, Trends and Perspective of Development. *Prog. Electromagn. Res. C* **2018**, *86*, 69–82. [CrossRef]
142. do Nascimento, V.C.; Moon, S.R.; Byerly, K.; Sudhoff, S.D.; Ohodnicki, P.R. Multiobjective Optimization Paradigm for Toroidal Inductors with Spatially Tuned Permeability. *IEEE Trans. Power Electron.* **2021**, *36*, 2510–2521. [CrossRef]
143. Li, Y.B.; Lei, G.; Bramerdorfer, G.; Peng, S.; Sun, X.D.; Zhu, J.G. Machine Learning for Design Optimization of Electromagnetic Devices: Recent Developments and Future Directions. *Appl. Sci.* **2021**, *11*, 1627. [CrossRef]

Disclaimer/Publisher's Note: The statements, opinions and data contained in all publications are solely those of the individual author(s) and contributor(s) and not of MDPI and/or the editor(s). MDPI and/or the editor(s) disclaim responsibility for any injury to people or property resulting from any ideas, methods, instructions or products referred to in the content.